

MODELLING OF RECOVERY AND RECRYSTALLIZATION IN MAGNESIUM ALLOYS

BY

PAWEL OKRUTNY, B.ENG.

A Thesis

Submitted to the School of Graduate Studies

in Partial Fulfilment of the Requirements

for the Degree

Master of Science

McMaster University

© Copyright by Pawel Okrutny, January 2011

MASTERS OF SCIENCE (2010)
(Department of Materials Science and Engineering)

McMaster University
Hamilton, Ontario

TITLE: Modelling of Recovery and Recrystallization in Magnesium Alloys

AUTHOR: Pawel Okrutny, B.Eng.

SUPERVISOR: Dr. Hatem Zurob (McMaster University) & Dr. Shahrzad Esmaeili
(University of Waterloo)

NUMBER OF PAGES: xiv, 101

Abstract

Through the study of recovery, precipitation and their effects on recrystallization at various annealing temperatures, a physically based model was developed to describe recrystallization kinetics of Mg AZ31. Based on Zener drag calculations, precipitates in AZ31 had little effect on recrystallization. Recovery activation energy and activation volume were determined from yield stress vs. time experiments. Recovery kinetics were used to determine the stored energy remaining within the material throughout the annealing process. Recrystallization experiments showed that contraction twins were preferred regions of recrystallization and in-situ recrystallization experiments showed that twin/twin and twin/GB intersections were ideal locations for nuclei growth outside of the twinned volume. Given the deformation and the annealing temperature, the proposed model is able to predict the recrystallized fraction as a function of time. Future versions of the model may be used to construct recrystallization-time-temperature (RTT) maps as well as predict recrystallized grain size after a time of anneal. The model predictions are in excellent qualitative agreement with experimental observations and can capture nucleation growth within both the twins and matrix

Acknowledgements

This thesis would not have been possible without the hard work and dedication of my master's supervisor Dr. Hatem Zurob. His encouragement, enthusiasm and immense knowledge bank were utilized heavily during this work. He *always* found time to answer questions or discuss concerns, albeit it at 6:00am in a coffee shop, or 6:00pm on a golf course. To him I also owe the privilege of being able to spend the last few months of my father's life by his side. For everything he has done for me I will be forever grateful. I was lucky to have him as my supervisor, and cannot image accomplishing as much as I have without him.

This thesis also could not have been possible without Dr. Yves Brechet. His great insight into virtually everything materials related played a significant role in this all encompassing model. He was the single biggest inspiration behind the equations governing the recrystallization model within the twinned volume. Furthermore, Dr. Shahrzad Esmaeili was exceptionally helpful with work pertaining to the precipitation within AZ31.

Of course, a great deal of the experimental results would not have been available without the hard work and dedication of Brick Kung who spent most of his summer adjacent to a hot furnace in order to move the research along. Brick's hard work helped move the research along in what turned out to be an extremely busy period in my life. I also have to thank Mohammad Kashif Ur Rehman, or simply 'Kashif', who contributed a great deal of discussion pertaining to the final stages of the model and managed to read one of the first versions of the thesis in order to help identify mistakes.

The grueling process of focusing on a single subject for an extended period of time would have been unbearable without the constant intellectual -distractions- provided by the many great people I met at McMaster. I was able to find a common conversation topic with virtually all grad students, support staff and faculty and was able to learn something from all I had come into contact with. All these spontaneous conversations will be dearly missed. The lab work would have been impossible without the input of the wonderful technicians we

have working at McMaster. Their busy schedules are instantly set aside when approached with a question and they will not stop working until it is solved.

Furthermore, without the input of support and encouragement from my family, I would not have been able to output the amount of energy and dedication necessary to undertake such a project. My parents would be around for me when I needed them and away from them when I needed the space, such comfort was extremely appreciated. I also need to thank my fiancée Marka for her patience with my busy schedule, her understanding of my needs, her attempt at making me eat healthy during my random schedule and her ability to make me enjoy my busy schedule and still be in touch with life. She also helped read the first version of the thesis, and helped force me, at several occasions, to finally get it done.

Finally, I wished to dedicate this thesis to two people. My dad *Ryszard Okrutny* and My supervisor *Dr. Hatem Zurob*. This thesis is for my dad because on the day before he passed away I asked him what I could do to repay him for being such a great father, his answer was that I had already done enough while referencing my education. And of course, I could not have achieved my thesis and been able to repay my father without the dedication of my supervisor Hatem Zurob. Thus, the thesis is dedicated to the two of you.

Table of Contents

Abstract	iii
Acknowledgements	iv
List of Figures	ix
List of Tables	xiv
Chapter 1 Preface	1
1.1 Introduction	1
1.2 List of Acronyms	3
Chapter 2 Literature Review	4
2.1 Magnesium and its Alloys	4
2.2 AZ31 Phase Diagrams	6
2.3 Deformation of Mg and AZ31	8
2.3.1 Deformation	8
2.3.2 Texture	13
2.4 Annealing	15
2.4.1 Formability	18
2.5 Recovery	20
2.5.1 Overview	20
2.5.2 Recovery in Mg Alloys	21
2.6 Recrystallization	23

2.6.1	General Recrystallization Overview	23
2.6.2	Recrystallization in Mg Alloys	25
2.7	Modelling	28
2.7.1	Recovery	28
2.7.2	Recrystallization	29
Chapter 3 Experimental Procedure		31
3.1	Experimental	31
3.1.1	Materials	32
3.1.2	Microstructure Characterization	32
3.1.3	Texture	33
3.1.4	Recovery	33
3.1.5	Recrystallization	34
3.1.6	Annealing	35
3.1.7	Transmission Electron Microscopy	36
Chapter 4 Results		38
4.1	Transmission Electron Microscopy	38
4.2	Recovery Experiments and Modelling	41
4.3	Texture	41
4.4	Recrystallization	47
4.4.1	‘Semi’ In Situ Recrystallization	49

Chapter 5 Discussion	55
5.1 Transmission Electron Microscopy	55
5.2 Nucleation Sites	58
5.3 Recovery	60
5.4 Modelling	61
5.4.1 Recrystallization	62
5.4.2 Recrystallization in Mg Alloys	63
5.4.3 Model	65
5.4.4 Model Input Parameters	80
5.5 Model Summary	85
5.6 Model Improvements	88
5.6.1 Precipitation	88
5.6.2 Grain Size	89
5.7 Recrystallization	90
5.7.1 ‘Semi’-in-situ Growth	91
5.7.2 Geometry Effects	93
5.7.3 Geometry Effects in Studied Samples	97
 Chapter 6 Conclusions and Future Work	 99
6.1 Conclusions	99
6.2 Future Work	100

List of Figures

2.1	The typical tensile strength and elongation for the most common commercial wrought magnesium alloys (solid symbols) and a number of experimental alloys (open symbols)	6
2.2	Phase diagram of AZ31 with 0.3% Mn as calculated with FactSAGE. . .	7
2.3	Schematic of different slip systems present in HCP AZ31	9
2.4	CRSS plotted versus temperature showing the high correlation of temperature with the number of active slip systems in Mg	10
2.5	Schematic of double twinning inspired by Reed-Hill	12
2.6	Initial texture found in AZ31 (a) commercially recrystallized sheet and (b) squeeze cast material. Texture after cold rolling of (c) commercially recrystallized sheet and (d) squeeze cast material. Styczynski et al. [2004]	14
2.7	Schematic image of the basal texture produced in Mg after cold rolling.	15
2.8	True stress-strain curves for AZ31 cold rolled and hot rolled at a constant strain rate of $1.3 \times 10^{-4} s^{-1}$	19
2.9	Mechanisms involved in the development of recrystallized grains. Reproduced in part from Drury and Humphreys [1985]	23
2.10	Typical recrystallization kinetics during isothermal annealing	24

4.1	a) Transmission Electron Microscopy (TEM) image of AZ31-ST-GG sample showing Al_8Mn_5 distribution throughout a grain. b) TEM image of post heat treatment and deformation sample AZ31-ST-GG-CR30pct-250C-1000s showing an unchanged Al_8Mn_5 distribution throughout a grain.	39
4.2	a) TEM image of AZ31-ST-GG and b) accompanying diffraction pattern. c) TEM image of AZ31-ST-GG post deformation and further heat treatment displaying signs of a small unidentified precipitate throughout the matrix. (Several instances of the new precipitate have been marked by arrows) and d) a diffraction pattern of the area highlighted in the black circle showing double reflection spots from the matrix indicating the existence of a new precipitate	40
4.3	Yield Stress vs Anneal time as predicted by model (solid lines) and by experimental results (points)	41
4.4	Intensity distribution of multiple (hkl) reflections taken from the raw data. a) AZ31 Solution Treated at $400^\circ C$ for 24h then heated to $400^\circ C$ for 2h to facilitate grain growth (AZ31-ST-GG) b) AZ31-ST-GG further rolled parallel to rolling direction and c) AZ31-ST-GG further rolled perpendicular to rolling direction	43
4.5	Basal plane pole figures established from texture measurements performed using a Bruker X-ray diffraction goniometer along the rolling direction with Cu $K\alpha$ radiation. The pole figure shows a solution treated ($450^\circ C$ for 24h) sample with grown grains ($\epsilon = 0.05, 470^\circ C$ for 2h). Numbers shown are times random.	43

4.6	Basal plane pole figures established from texture measurements performed using a Bruker X-ray diffraction goniometer along the rolling direction with Cu $K\alpha$ radiation. Starting texture shown in Fig. 4.5: a) Rolling along original rolling direction b) Rolling perpendicular to original rolling direction c) Rolling in various ways to the rolling direction. Numbers shown are times random.	44
4.7	$\langle 10\bar{1}1 \rangle$ plane pole figures established from texture measurements performed using a Bruker X-ray diffraction goniometer along the rolling direction with Cu $K\alpha$ radiation. The pole figure shows a solution treated ($450^{\circ}C$ for 24h) sample with grown grains ($\epsilon = 0.05$, $470^{\circ}C$ for 2h). Numbers shown are times random.	44
4.8	$\langle 10\bar{1}1 \rangle$ plane pole figures established from texture measurements performed using a Bruker X-ray diffraction goniometer along the rolling direction with Cu $K\alpha$ radiation. Starting texture shown in Fig. 4.7: a) Rolling along original rolling direction b) Rolling perpendicular to original rolling direction c) Rolling in various ways to the rolling direction. Numbers shown are times random.	45
4.9	Recrystallized volume fraction at different temperatures comparing different rolling directions and their affect on recrystallization. Samples were rolled either parallel to rolling direction marked as RD, or alternated between perpendicular and parallel rolling directions marked as AD.	48
4.10	Recrystallized volume fraction with samples cold rolled to $\epsilon = 0.1$ of equivalent strain. Samples were rolled parallel to rolling direction.	49

4.11	Microstructure evolution of the same area during recrystallization of 30% cold rolled AZ31 at 200°C after a) 3s of annealing b) 30s of annealing c) 100s of annealing d) 1200s of annealing	51
4.12	Microstructure evolution of the same area during recrystallization of 30% cold rolled AZ31 at 250°C after a) 30s of annealing b) 100s of annealing c) 300s of annealing d) 1200s of annealing	52
4.13	Microstructure evolution of the same area during recrystallization of 30% cold rolled AZ31 at 300°C after a) 3s of annealing b) 10s of annealing c) 30s of annealing d) 250s of annealing	53
4.14	Long time annealing of 200°C sample cold rolled to $\epsilon = 0.3$ for a) 16 hours b) 48 hours	54
4.15	Pre anneal a) and post anneal b) images of the same area showing favourable nucleation mechanisms within a $\epsilon = 0.3$ cold rolled sample annealed at 300°C for 30s. 1) Nucleation inside twins 2) Twin/twin intersection 3) Twin/GB intersection	54
5.1	a) 5s anneal b) 10s anneal capturing the most favourable nucleation mechanisms within a $\epsilon = 0.1$ cold rolled sample annealed at 275°C	59
5.2	Tensile sample grip sections after a 150°C anneal for a) 0min b) 25min c) 90min showing no signs of recrystallization or any other microstructural changes throughout the recovery process	61
5.3	Grain size distribution based on the Rayleigh distribution function	66

5.4	As the value of $\chi_{c(HAGB)}$ decreases with increasing annealing time a larger portion of sub-grains become HAGBs. Images (a) and (b) display the fraction of created HAGBs within the twinned region. $\sim 10\%$ in a) showing the start of recrystallisation $\sim 30\%$ in b)	68
5.5	r_c changing with time. In a) r_c always grows faster than $\langle r(t) \rangle$ and no bulging happens, however in b) after a period of growth, $\langle r(t) \rangle$ overcomes and surpasses r_c allowing for bulging to take place. Reproduced from Dunlop et al. [2006]	76
5.6	Recrystallization data compared to modelling results obtained using parameters listed in Table 5.5.	81
5.7	Comparison of ideal HAGB mobility as calculated by Turnbull with fitted HAGB mobility.	84
5.8	Model flowchart pertaining to recrystallization within the twin	86
5.9	Model flowchart pertaining to recrystallization within the matrix	87
5.10	Comparison between random and non-random distribution of nuclei	96
5.11	Microstructure evolution of the same area during recrystallization of 30% cold rolled AZ31 at 250°C after a) 3s of annealing b) 100s of annealing c) 300s of annealing d) 1200s of annealing. The direction lines on b) c) and d) show the predicted grain growth directions based on the initial twin intersection where a nuclei formed.	98

List of Tables

3.1	Material Composition Magnesium AZ31	32
5.1	Precipitation analysis in AZ31 before and after heat treatment.	57
5.2	Calculated activation energy and activation volume	61
5.3	Four rate equations describing the evolution of the Minkowski functionals for recrystallization and their geometrical significance	71
5.4	Four rate equations describing the evolution of the Minkowski functionals for recrystallization and their geometrical significance	78
5.5	Model Input Parameters	80
5.6	LAGB to HAGB mobility ration at various temperatures	83
5.7	Time exponent during different types of growth	95

Chapter 1

Preface

1.1 Introduction

Due to its low density, magnesium and its alloys have recently caught the attention of many automotive designers as an optimal structural material for automotive parts. Reducing vehicle weight by using high strength, low density materials for structural components is an attractive approach to increasing their fuel efficiency. Lighter vehicles require smaller suspensions, breaks and engines, all of which contribute to lowering the total vehicle weight and increasing fuel efficiency.

Alongside the many benefits, there are difficulties with using magnesium as an industrial material due to its low formability at room temperature. This arises from the limited number of slip systems available in HCP magnesium alloys at room temperature.

The limitation of having few slip systems is further complicated by magnesium's tendency to develop and retain a strong texture during deformation. After rolling, a strong basal texture is present in magnesium. As an HCP material, the $\langle 0001 \rangle$ plane should be the slip plane of choice. However, in magnesium alloy AZ31 with basal texture, this plane becomes completely parallel to the rolling direction within many grains making deformation in the thickness direction difficult. During most rolling and forging operations with Mg, twins and double twins are formed which contribute to the shape change and increase in strength.

Twins have been reported to be responsible for creating dislocation inhomogeneity within the matrix and trapping dislocations within the twinned volume. Bhattacharyya et al. [2009] found dislocation debris inside twins. This debris is that of dislocations which existed within the matrix before twinning. These dislocations became trapped after the twin rotated the matrix. This debris of trapped dislocations was found to cause a dislocation-rich structure within the twins that is likely to contribute to work hardening [Bhattacharyya et al., 2009]. Such stored residual stresses spread heterogeneously throughout the material can lead to changes in many macroscopic properties through grain refinement. Grain refinement happens during annealing operations carried out to relieve the residual stresses via recovery and recrystallization. Since forming recrystallization nuclei is most favourable in areas of highest stored energy and misorientation, twins are good candidates for nucleation of recrystallized grains.

Static recovery and static recrystallization appear to be viable methods for removing the stresses caused by forging operations. Unfortunately, their behavior in magnesium is not fully understood. A model which can capture correctly magnesium's static recovery and static recrystallization kinetics is of utmost importance in order to predict the macroscopic properties of magnesium products. This model would also benefit the understanding of the mechanisms involved in both recovery and recrystallization phenomena.

The goal of this work was to develop such a model. The model developed was a coupled recovery and recrystallization model in which recrystallization starts rapidly within the twins and continues by nucleating on specific parts of the material such as grain triple junctions and twin/grain intersections.

1.2 List of Acronyms

AZ31-ST AZ31 Solution Treated at 400°C for 24h

AZ31-ST-GG AZ31 Solution Treated at 400°C for 24h then heated to 400°C for 2h to facilitate grain growth

AZ31-ST-GG-CR30pct-250C-1000s AZ31 Solution Treated at 400°C for 24h then heated to 400°C for 2h to facilitate grain growth then cold rolled $\epsilon = 0.3$ and annealed at 250°C for 1000s

TEM Transmission Electron Microscopy

CRSS Critically Resolved Shear Stress

LAGB Low Angle Grain Boundary

HAGB High Angle Grain Boundary

Chapter 2

Literature Review

2.1 Magnesium and its Alloys

The improvement of extraction methods coupled with the fact that magnesium is the sixth most abundant element on earth by wt% [Skinner, 1979], magnesium is poised to be an important structural material in the future. In addition to being abundant, magnesium is the lightest structural metal with a specific density of $1.74 \frac{g}{cm^3}$, about two thirds that of aluminum, $2.7 \frac{g}{cm^3}$, and one quarter that of iron, $7.874 \frac{g}{cm^3}$. Therefore, magnesium has caught the attention of many automotive designers who wish to use it as a structural material for automotive parts. Reducing vehicle weight by using high strength, low density materials for structural components is an attractive approach which increases fuel efficiency. Furthermore, lighter vehicles require smaller suspensions, breaks and engines, all of which will contribute to lowering the total vehicle weight and increasing fuel efficiency. It is estimated that a 10% reduction in vehicle mass translates to an increase of 6-7% in fuel economy [Canada, 2002]. Automotive parts produced from magnesium are also highly recyclable, consuming only 5% of the energy during recycling compared to the production of the primary metal [Czerwinski, 2007].

Mg can be produced by electrolysis from $MgCl_2$ as first demonstrated by Robert Bunsen in 1852. It can also be produced via the Pidgeon process where $Si_s + MgO_s \rightleftharpoons SiO_{2s} + Mg_g$. This reaction is thermodynamically unfavourable at low temperatures,

however with the addition of heat result in the reduction of MgO. Countries that have an abundant supply of clean energy are most favorably set up to produce Mg. In the past, Canada was one of the world's top producers of Magnesium. Recently however, China has taken the lead. Though with further research and investment, Canada can once again be at the forefront of this novel structural material.

Pure magnesium is rarely used as a structural material. The vast majority of magnesium structural components are commercial alloys containing Al, Ag, Mn, Zn, Zr and rare earths.

These alloying elements are added to influence either corrosion behavior, physical or mechanical properties, weldability, and machinability. The following alloying properties are taken from Davis [2001]:

Aluminum: Enhances a multitude of properties such as castability, hardness and strength. At higher percentages (>6%) Al allows Mg alloys to be heat treatable.

Zinc: Zinc is often used in combination with Al to improve ambient temperature strength.

Manganese: Manganese does not change the physical strength of Mg. It is typically found as an artifact left over from the removal process of iron and other heavy metals from the melt.

Iron: Iron is typically the least desired element found within Mg and is typically present as an impurity. It is undesired as even small amounts of iron (0.005 wt%) can significantly reduce corrosion resistance.

Calcium: Similar to Zinc, Calcium is added to reduce oxidation. Calcium, however, is more effective at reducing oxidation during the molten state throughout production.

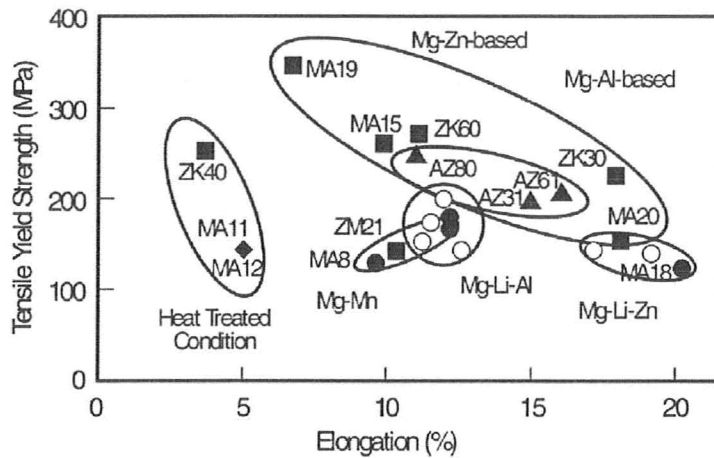


Figure 2.1: The typical tensile strength and elongation for the most common commercial wrought magnesium alloys (solid symbols) and a number of experimental alloys (open symbols)

Copper: Copper adversely affects the corrosion resistance of magnesium but improves room and high temperature strength.

Based on the elements listed, many multipurpose alloys can be created covering a large spectra of yield strength and elongation space as seen in Figure 2.1 produced by Bettles and Gibson [2005]. Alloy AZ31 was chosen for this study because it is both highly studied and formable. This alloy is composed of 3 wt% Al and 1 wt% Zn with the remainder Mg.

2.2 AZ31 Phase Diagrams

In order to determine if significant phase changes occur during the temperatures where recovery and recrystallization will be studied, a phase diagram for AZ31 was consulted. The phase diagram was produced using FactSAGE software using its light metals database and assuming that AZ31 was composed of 3% Al and 1% Zn with the

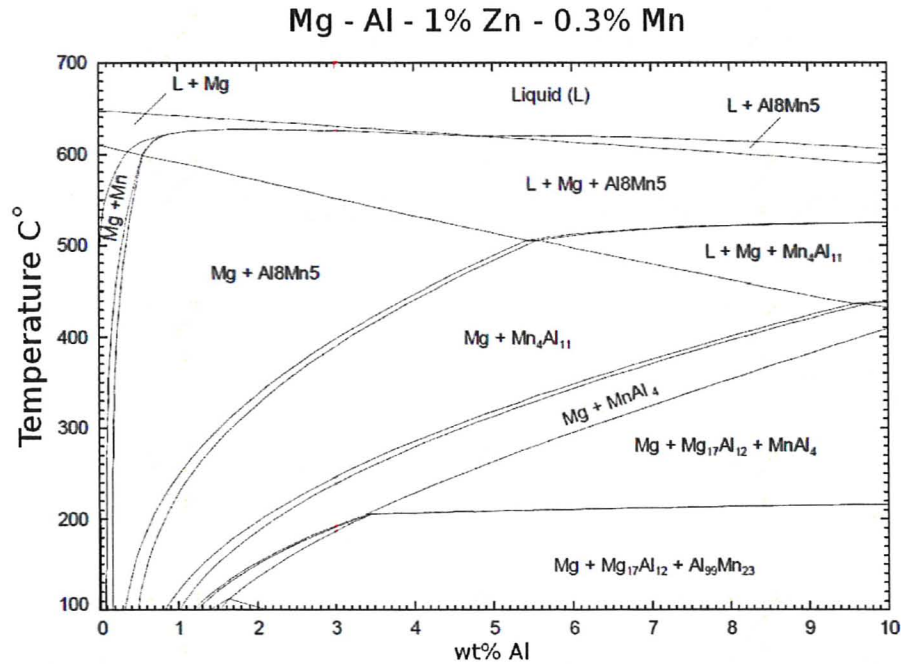


Figure 2.2: Phase diagram of AZ31 with 0.3% Mn as calculated with FactSAGE.

remainder Mg containing Mn as an impurity. If impurities are not considered, an AZ31 phase diagram predicts a homogeneous material after solution treatment at 400°C , however, in reality this is not the case. Multiple TEM studies show precipitate particles throughout the microstructure. These particles result from impurities present in commercial alloys. One of the most prevalent elements in commercial purity AZ31 is Mn, present as an artifact left over from the removal process of iron and other heavy elements. A complete representation of the phases present in the commercial grade AZ31 is shown in Figure 2.2 which is a modified version of the one produced in the FactSAGE Alloy Design workshop in Montreal 2010.

Figure 2.2 accurately predicts that precipitates will be present after a solution treatment at 450°C for 24 hours as the Al_8Mn_5 phase is stable well above the solidus. Since a solution treatment anneal is ineffective at dissolving the Al_8Mn_5

phase at room temperature, it is possible that the Al_8Mn_5 phase is present across the microstructure throughout many annealing treatments.

2.3 Deformation of Mg and AZ31

2.3.1 Deformation

Although there are many benefits, there are also difficulties with using magnesium as an industrial material due to its low formability. The low formability arises from the limited number of slip systems available in HCP magnesium alloys at room temperature [Agnew et al., 2001]. At low temperatures, slip on $\{0001\}\langle 11\bar{2}0 \rangle$ is the dominant slip mode due to its low Critically Resolved Shear Stress (CRSS) [Roberts, 1960].

The $\langle 11\bar{2}0 \rangle$ direction is also found on the prism plane $\{10\bar{1}0\}$ and the pyramidal plane $\{10\bar{1}1\}$ shown in Figure 2.3. It is possible to have slip in magnesium on $\{10\bar{1}0\}\langle 11\bar{2}0 \rangle$ and $\{10\bar{1}1\}\langle 11\bar{2}0 \rangle$, which is referred to as prismatic slip and pyramidal slip, respectively [Gottstein and Samman, 2005]. However, prismatic and pyramidal slip systems both have a much larger CRSS than basal slip and can be thought of as less preferred slip systems.

Basal, prismatic and pyramidal slip systems have their slip direction within the basal plane and cannot accommodate deformation out of the basal plane. Therefore, to accommodate a deformation perpendicular to the basal plane a crystal is more likely to deform by mechanical twinning.

The type of twins that arise from a cold rolled AZ31 sheet with a basal texture are of type $\{10\bar{1}1\}$. The $\{10\bar{1}1\}$ twin are seen to act as a complementary deformation

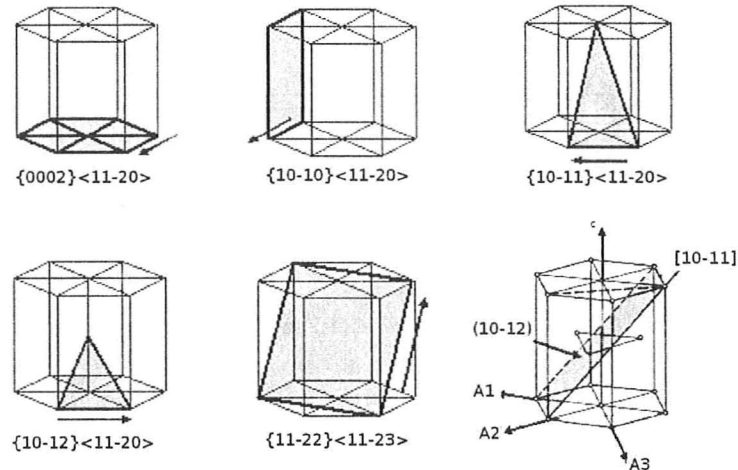


Figure 2.3: Schematic of different slip systems present in HCP AZ31

mechanism which accommodates contraction in the c -direction and have been called contraction twins. Twins however, have a drawback. Gottstein and Samman [2005] found that initially mechanical twinning was able to accommodate applied strain, however, since twinning would reorient the basal plane close to the compression plane the material failed to accommodate larger degrees of deformation.

Figure 2.4 is a compilation of the CRSS for different deformation modes in Mg. The figure compiled by Hiura [2010] shows different independent deformation modes active at room temperature. For the purpose of cold rolling, the figure is deceiving as it shows $\{0001\}\langle 2\bar{1}\bar{1}0\rangle$ basal slip and $\{10\bar{1}2\}$ twins as relatively easy deformation modes while it does not account for the difficulty of these deformation modes to accommodate cold rolling in a material with a highly defined texture. A material with a basal texture, for example, will have the $\{0001\}$ plane perpendicular to the c -direction and basal slip will be difficult. In the same texture situation, pyramidal and prismatic slip will also be ineffective for cold rolling and grains will be forced to deform by $\{10\bar{1}1\}$ twinning. In fact $\{10\bar{1}1\}$ twins have been named ‘contraction’ twins due to their prevalence after cold rolling of basal textured magnesium. During cold

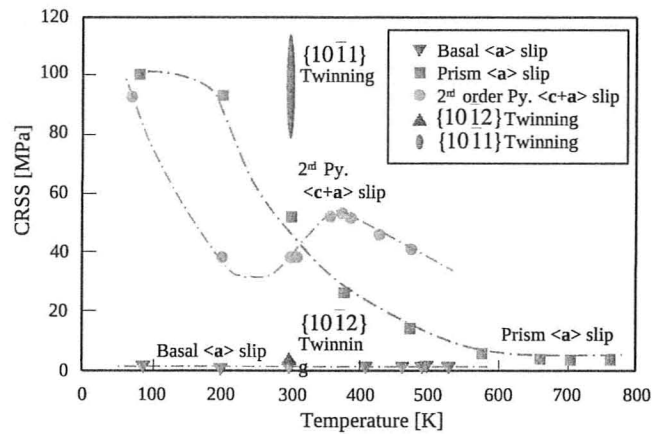


Figure 2.4: CRSS plotted versus temperature showing the high correlation of temperature with the number of active slip systems in Mg

rolling of AZ31 material with a basal texture, the expected twins that arise will be $\{10\bar{1}1\}$ contraction twins and $\{10\bar{1}1\} - \{10\bar{1}2\}$ double twins as predicted by the work of Wonsiewicz and Backofen [1967]. As such, these twins will be primarily focused on during the subsequent work as they are responsible for accommodating the cold rolling strain.

The process of deformation twinning is in short a realignment of the original crystal structure into a new orientation during an applied stress. A material can deform by either slip or twinning and the difference between the two mechanisms is that in the former, deformation occurs on the individual lattice planes and in the latter, the shear is distributed over a volume.

Deformation twins typically form by a uniform simple shear of the parent lattice. This shear produces an array of highly co-ordinated atom displacements which can accommodate an applied external stress [Christian, 1995]. In most crystalline solids,

twinning is a method of plastic deformation only at high strain rates or low temperatures. However, since some HCP metals such as Mg lack the appropriate number of deformation systems, twinning is necessary to maintain plastic flow [Christian, 1995]. This twin activity attributable to the strong increase of CRSS for all slip systems with decreasing temperature compared to the athermal nature of the CRSS for twinning and is applicable to Mg alloys such as AZ31.

During deformation twinning, very high stresses can be found around the vicinity of the twin most specifically in the adjacent grains. These stresses and associated strain energies are produced by the resistance of the matrix to the macroscopic shape change in the twinned volume [Christian, 1995]. Although twinning produces high local strain, twins can also act as an efficient way to accommodate an externally applied load and are an important part of Mg deformation. Su et al. [2008] noted that AZ31 first deforms by slip; however, further acts of deformation rapidly require twinning to accommodate slip.

Twins in Mg are also known to cause another phenomenon during general plastic flow. During twinning, those grains which are initially unfavorably oriented for slip can be reoriented into a direction more favorable for slip via the process of double twinning [Yoo, 1981]. The process of double twinning in Mg alloys starts by the $\{10\bar{1}1\}$ twin. The $\{10\bar{1}1\}$ twin rotates the twinned volume to 56.2° with respect to the untwinned matrix. Next, within the same twinned region, a $\{10\bar{1}2\}$ twin is created rotating back the doubly twinned region to a final rotation of 37.5° from the untwinned matrix. In order to visualize the process, Reed-Hill [1960] produced Figure 2.5 which shows a visual schematic of double twinning. The process of double twinning is commonly reported in AZ31 during cold deformation [Barnett et al., 2004, Al-Samman and Gottstein, 2008, Barnett et al., 2005, Wonsiewicz, 1966] indicating that it is an important part of the deformation mechanism.

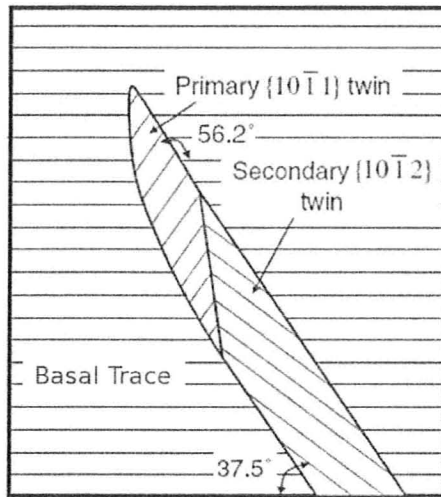


Figure 2.5: Schematic of double twinning inspired by Reed-Hill

During double twinning, the secondary twin rotates the grain into a position more favourable for slip and because of this rotation the total plastic strain can increase considerably [Yoo, 1981]. These double twin rotations allow for a great deal of slip activity within the twin volume during deformation. This increase in slip activity within only some grains produces stored energy heterogeneity throughout the material [Myshlyaev et al., 2002, Kelley and Hosford, 1968] Hartt and Reed-Hill [1968], showed that although twinned single crystals may fracture at a macroscopic strain of less than 1%, the shear strains occurring within the twin bands can be up to 1000%.

Upon formation, twins have also been reported to be responsible for creating debris and trapping initially glissile dislocations within the twinned volume turning them into sessile dislocations through grain rotation. Bhattacharyya et al. [2009] found left over debris inside twins formed from original dislocations which existed within the matrix before twinning and were trapped after the twin rotated the matrix. This debris of trapped dislocations was found to cause a dislocation-rich structure within the twins that is likely to contribute to work hardening Bhattacharyya et al. [2009].

Since the stored energy within grains is a function of dislocation density, grains with a higher dislocation density will maintain a higher stored energy. Such stored energy can lead to changes in many macroscopic properties through grain refinement during annealing operations.

It is important to note that the activity of any particular slip mode including a twin system depends heavily on the orientation of the crystal. A randomly textured material would allow deformation to take place on at least some grains and substantially increase formability, while a strong texture lowers formability by eliminating potential deformation modes on a majority of the grains. In fact, the goal of many studies that aim to increase the formability of Mg is to randomize the texture. Thus, it is important to be familiar with the starting texture of Mg alloys before deformation.

2.3.2 Texture

Texture within a material is the distribution of crystallographic orientations within a polycrystalline sample. Since in a highly textured material all of the grains contain a specific orientation, the deformation of this material will highly depend on this specific orientation's ability to accommodate slip. A number of studies have focused on the origin of the cold rolling texture in Mg alloys and they are summarized in this section.

The cold rolling texture in HCP metals strongly depends on the c/a ratio [Agnew et al., 2001]. Pure magnesium has a c/a ratio of 1.622, approaching that of the ideal c/a ratio at 1.633 and thus after cold rolling a basal texture is commonly observed [Styczynski et al., 2004]. The same texture behavior is observed for magnesium's alloys including AZ31. Styczynski et al. [2004] investigated two types of AZ31 mag-

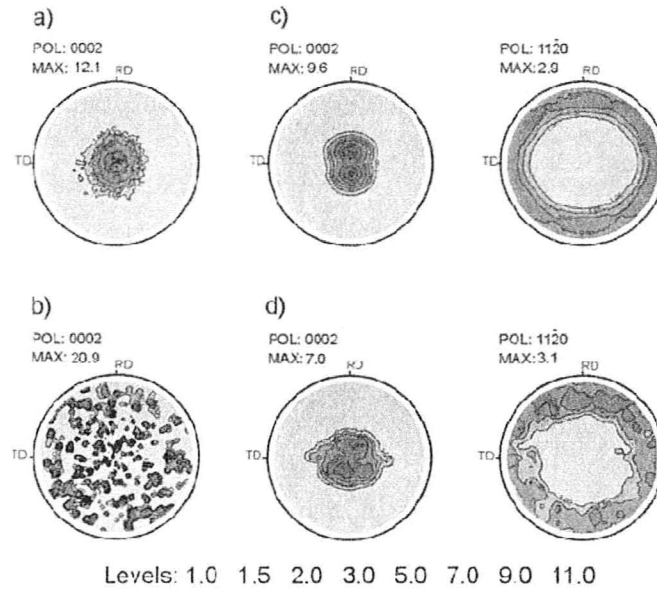


Figure 2.6: Initial texture found in AZ31 (a) commercially recrystallized sheet and (b) squeeze cast material. Texture after cold rolling of (c) commercially recrystallized sheet and (d) squeeze cast material. Styczynski et al. [2004]

nesium alloys corresponding to different microstructure conditions, the first was a commercially recrystallized sheet and the second one was a squeeze cast bar. They recorded predeformation textures, then cold rolled and recorded postdeformation texture in both alloys. The results of their study are shown in Fig. 2.6, where (a) and (b) are initial textures of recrystallized sheet and squeeze cast material respectively and (c) and (d) are the cold rolling textures for the same alloys. Through their work, Styczynski et al. [2004] have shown that regardless of starting microstructure, after cold rolling a strong basal texture is present in Mg AZ31.

A schematic of the post cold rolled basal texture is shown in Fig.2.7 which is based on the original schematic produced by Jain [2010]. As shown, the cold rolled texture in HCP metals has the c-axis perpendicular to the rolling direction and the basal plane $\{0001\}$ parallel to the rolling direction. As discussed in the previous section, the basal

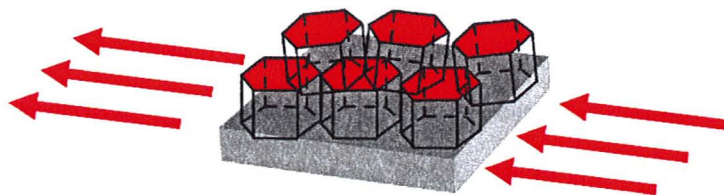


Figure 2.7: Schematic image of the basal texture produced in Mg after cold rolling.

plane should be the slip plane of choice in AZ31 due to its low CRSS, however, this plane becomes parallel to the rolling direction after rolling. A basal texture is thus undesirable as it places grains in an orientation not suited for deformation by making the resolved shear stress in the basal plane practically zero. Therefore, once a basal texture is present in AZ31, the material is no longer favourably oriented for slip and twinning becomes an important deformation mechanism.

In a material with a basal texture, twinning has a significant impact on the formability. Al-Samman and Gottstein [2008] investigated five different starting textures in an AZ31 alloy while deforming at room temperature. The various samples were produced in such a way that the activation of slip on the basal plane was either enhanced or suppressed. Their findings show that in the case where the basal planes were parallel to the compression direction, a zero resolved shear stress was produced causing basal slip to be totally suppressed. When basal slip was suppressed, non-basal slip or twinning would dominate the start of deformation and reorient grains into orientations more favourable for slip Al-Samman and Gottstein [2008].

2.4 Annealing

During annealing, grain refinement may occur as a result of recrystallization, which is a process where new deformation free grains are formed in highly deformed

regions in order to relieve stored energy. It is most favourable to form recrystallization nuclei in areas of highest stored energy and as such, twins are an excellent nucleation site. Recrystallization nuclei within twins have been reported by several authors [Barnett et al., 2005, Su et al., 2008, Sitdikov et al., 2003, Beer and Barnett, 2007]. All authors agree that recrystallization nuclei tend to start in those areas since the driving force for recrystallization is highest.

By examining different annealing conditions, Li et al. [2009] found that contraction twins are a favourable nucleation site for recrystallization. Although it is generally assumed that compression twin boundaries are not very mobile, atomic interaction during deformation can destroy the immobile boundaries allowing for the growth to take place [Li et al., 2009].

The mechanism of recrystallization within twins has been considered by Sitdikov et al. [2003] in their work on dynamic recrystallization in Mg. They found multiple stages to the process of recrystallization within the twin volume. The process begins with the rearrangement of lattice dislocations within the twin lamellas. It is then followed by the development of High Angle Grain Boundaries (HAGBs) which form recrystallization nuclei and is followed by the migration of these HAGBs into recrystallized grains.

The multiple stage recrystallization kinetics taking place in magnesium during which recrystallization in twins is more rapid than within the matrix is very likely to lead to deviations from the typical sigmoidal recrystallization kinetics. After metallographic work on the recrystallized microstructure Li et al. [2009] was able to confirm that the recrystallization kinetics in magnesium do not follow the typical sigmoidal curve.

A great deal of work can be found on the dynamic recrystallization (DREX) behaviour of Mg and Mg alloys. Dynamic recrystallization is the creation and growth of new deformation free grains during an applied load at elevated temperatures. In contrast to DREX, static recrystallization (SREX) is where new dislocation-free grains are created during a subsequent anneal after deformation. Although static recrystallization is of primary interest to this project, a greater amount of literature data pertains to DREX some of which is mentioned in the subsequent part of this section.*

Recent work on dynamic recrystallization within magnesium showed that deformed magnesium has a significant twin volume fraction containing a large amount of stored energy and that new grains are formed progressively within these deformed regions from the continuous growth of subgrains [Beer and Barnett, 2007]. As subgrains grow they increase in misorientation and this increase in misorientation leads to the formation of HAGBs. The formation of new dislocation free grains increases the formability of Mg alloys and thus it can be a highly desirable feature.

The key ideas from this literature review so far are: *a)* twins can rotate the matrix into positions favourable for slip; *b)* while rotating the matrix twins can 'trap' glissile dislocations causing them to become sessile; *c)* these twinning induced rotations cause the twinned regions to accommodate a greater portion of slip and at the same time store a larger amount of deformation energy, and; *d)* subgrain boundary growth leads to an increase of misorientation creating HAGBs within the twins resulting in a favourable site for recrystallization nucleation.

*Literature overall contains more data on DREX since a large amount of industrial processes deform magnesium at high temperatures producing a higher interest in the study of DREX. Also, static recrystallization experiments are difficult to perform as they require the material to be deformed to high strains at low temperatures, something difficult to accomplish in Mg

2.4.1 Formability

AZ series Mg alloys composed of Mg-Al-Zn(Mn) are currently most commonly used in wrought applications due to their relative ease of extrusion and adequate mechanical properties, but they suffer from a relatively narrow processing window [Bettles and Gibson, 2005]. As such, there is great interest in the high temperature formability of magnesium and/or the removal of its strong basal texture.

High temperature reduces the CRSS necessary for slip to take place and activates more slip systems, thereby ductility and ease of production are highly improved [Chabbi et al., 2001]. Working at high temperatures facilitates the deformation of these alloys by increasing ductility and lowering the yield strength as shown in Figure 2.8, allowing complicated shapes to be forged [Jäger et al., 2004]. Ductility is improved at high temperatures mainly as a result of the activation of non-basal slip systems as well as dynamic recovery and recrystallization. Unfortunately, hot deformation is an energy intensive procedure with its own issues such as high cost, oxidation and its inability to produce very precise components due to thermal expansion and contraction.

An alternative to hot deformation is a batch process consisting of several small deformation steps each followed by an appropriate annealing step. Such a procedure can eliminate several of the issues with magnesium forging. Small deformations are preferred as after every deformation step, the material eliminates its internal stress by annealing. Static recovery and static recrystallization are the phenomena which would be responsible for removing stress caused by deformation.

More importantly, recrystallisation in most materials provides an opportunity to modify texture. As mentioned earlier, basal texture is undesirable as it places a large number of grains in an orientation not suited for deformation by rolling. Any modifi-

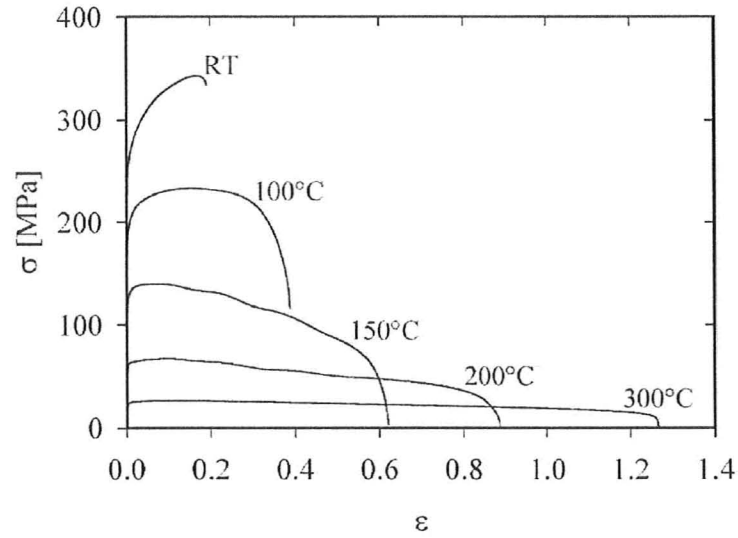


Figure 2.8: True stress-strain curves for AZ31 cold rolled and hot rolled at a constant strain rate of $1.3 \times 10^{-4} s^{-1}$

cation of the basal texture into one that is more random would increase formability. It is therefore important to understand the mechanisms of recrystallisation in AZ31 and its effect on texture as this may permit the development of a material with a weaker basal texture and thus improve formability.

Therefore, a model which can capture static recovery and static recrystallization is of utmost importance in order to understand and predict the behaviour of recrystallization within magnesium products and improve their formability.

2.5 Recovery

2.5.1 Overview

In a recent review of the subject, recovery was defined as all the annealing processes occurring in deformed materials without involving the migration of a high angle grain boundary [Doherty et al., 1997]. Recovery involves dislocation annihilation and rearrangement. In high stacking fault materials, subgrains develop and decrease the dislocation density by subgrain migration.

The phenomenon of recovery is difficult to directly observe due to the physically small size of individual dislocations. However, since the recovery process is accompanied by a change in physical properties recovery kinetics are often measured experimentally by following the change in either hardness, yield stress, resistivity or heat evolution.

As the density of dislocations changes, so do the aforementioned physical properties of the material. The forest hardening relation correlates yield stress to dislocation density ρ . It shows that the increase in yield stress is proportional to the square root of the dislocation density without influence of the dislocation distribution:

$$\sigma_{ys} = \sigma_o + M\alpha Gb\sqrt{\rho} \quad (2.1)$$

where M is the Taylor factor, G the shear modulus, b the Burgers vector and α is a dimensionless number close to 0.3. The difference between a deformed sample σ_{ys} and its initial undeformed state σ_o is assumed to only be dependent on $\sqrt{\rho}$ [Nes, 1995, Verdier et al., 1998]. The degree of recovery can thus be predicted by the change in

yield stress, a macroscopic property that can be easily measured by experiment or predicted in advance using a physically based model.

Through his work on Al-Mg alloys, Verdier et al. [1998] was able to successfully create a physically based model to relate the yield stress evolution during recovery. Their model uses a forest type hardening equation combined with relaxation driven by the motion of dislocations in their own average internal stress field. This recovery model was used in this work to predict recovery of AZ31.

Recovery is thermally activated and becomes increasingly faster at higher temperatures. For this reason, at high temperatures recovery and recrystallization begin to compete for the stored energy within the matrix. But one should keep in mind that their interaction is not purely described in terms of competition as recovery is needed to produce nuclei for recrystallization.

2.5.2 Recovery in Mg Alloys

To utilize Mg as a structural material, it becomes imperative to investigate its recovery kinetics. Recovery can significantly reduce yield strength during service life and as such, if Mg is to be a structure material, recovery kinetics need to be understood. Further reason to study recovery is due to its competitive yet vital relationship with recrystallization. Recovery kinetics are especially needed when trying to predict recrystallization.

Despite the important role recovery can play during material processing, it is a phenomena that is often overlooked. Recovery in Mg-Al-Zn has not been studied thoroughly in part due to the limited deformation capabilities of Mg-Al-Zn at low temperatures. In order to study recovery, it is necessary to create and store a great deal of defects within the matrix. In order to accomplish this, the matrix needs to

be deformed to high strains at low temperatures and such a combination produces inherent difficulties for Mg. As such, only limited data can be found on static recovery for Mg alloys deformed at room temperature [Su et al., 2008], [Shamsi et al., 2009].

To avoid the difficulty of deforming magnesium at room temperature, many groups studied dynamic recovery of magnesium at elevated temperatures. Dynamic recovery happens when a material is being deformed at an elevated temperature. The high temperatures are able to overcome the activation energy necessary for recovery to take place and allow a material to dynamically relieve stored energy while subject to further deformation.

Studying dynamic recovery is key to understanding the mechanisms which lead to recrystallization. During their studies on dynamic recrystallization, Drury and Humphreys [1985] proposed a mechanism that causes new recrystallized grains to form. They claim that two major processes are responsible for the transformation of subgrains into recrystallized grains during the process of dynamic recrystallization in magnesium. The first process is subgrain rotation where subgrains rotate and grow increasing their misorientation leading to the production of HAGBs as illustrated in Figure. 2.9(A). The second process of HAGB growth is strain induced grain boundary migration where grain boundaries migrate or *bulge* into another grain with a higher dislocation density as illustrated in Figure. 2.9(B). The initial subgrain boundary migration which leads to both boundary misorientation and bulging is believed to be promoted by large gradients of strain and orientation, such as those seen in deformation bands and twins [Drury and Humphreys, 1985].

Recent work by Bhattacharyya et al. [2009] on single magnesium crystals gives clues as to why such large orientation gradients may be present within twins. During their work, Bhattacharyya et al. [2009] noticed that a-type slip can be activated on multiple planes. This a-type slip produces a series of glissile dislocations which should

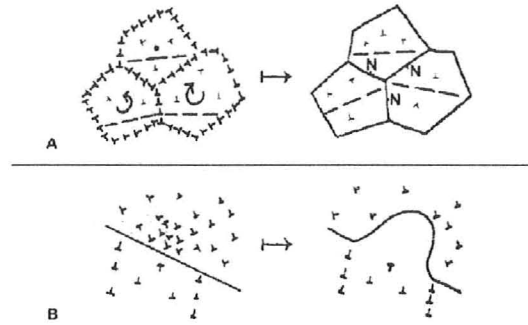


Figure 2.9: Mechanisms involved in the development of recrystallized grains. Reproduced in part from Drury and Humphreys [1985]

be able to recover easily. However, as deformation continues, a large volume fraction of the matrix is rotated by twinning and these a-type glissile dislocations are transformed due to this rotation to form sessile dislocations [Bhattacharyya et al., 2009]. These sessile dislocations are impossible to get rid of by simple glide and the twinned areas of the material can be expected to contain higher misorientation gradients. The trapped dislocations within the twins act as debris which leads to a dislocation-rich structure within the twins that is likely to contribute to work hardening [Bhattacharyya et al., 2009] and therefore a higher stored energy within the twinned fraction which can only be relieved by recrystallization.

2.6 Recrystallization

2.6.1 General Recrystallization Overview

A recent definition of recrystallization was provided by Doherty et al. [1997] and defines recrystallization as, “the formation of a new grain structure in a deformed material by the formation and migration of HAGB driven by the stored energy of

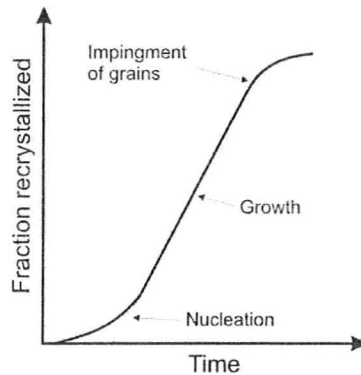


Figure 2.10: Typical recrystallization kinetics during isothermal annealing

deformation.” In other words, new grains are formed while consuming old grains which had a high stored energy. This high energy grain consumption in turn lowers the overall stored energy of the material.

Recrystallization determines the average grain size of wrought materials and the effects of grain size are significant in determining physical properties such as yield strength and creep kinetics. Therefore, it is of interest to understand recrystallization behaviour fundamentally in order to create models that can predict recrystallization kinetics and resulting grain sizes. These resulting grain sizes can then be used to predict other important fundamental material properties.

The kinetics of recrystallization commonly follow the profile shown in Figure 2.10. The recrystallized volume fraction (f_v) starts with an initial incubation period during which recovery slowly creates the first few nuclei. The new grains grow until all of the deformed material is consumed. These recrystallization kinetics are prevalent in various materials and a great deal of them are summarized in Humphreys and Hatherly [1995].

The volume fraction of recrystallized grains can be found using equation 2.2

$$f_{v_x} = F\dot{N}G^3dt^4 \quad (2.2)$$

where \dot{N} is composed of N nuclei that form in the time increment dt , G is the stored energy, t is time and F is the shape factor of the grains. For simplicity, grains that grow are often assumed to be spherical leading to a shape factor (F) to equal $\frac{4\pi}{3}$.

Equation 2.2 is accurate in predicting a spherical volume fraction, however it is only valid in the early stages of recrystallization when $f_v \ll 1$. Eventually the number of nuclei appearing in a time interval dt becomes less than $\dot{N}dt$ since nuclei cannot form in those parts of the specimen which have already recrystallized and equation 2.2 predicts recrystallization values that are too high. To account for this, the Avrami equation is derived by removing the effect of phantom nuclei (*nuclei which would have formed had appropriate space been provided*) For a complete derivation of Equation 2.3 the reader is directed to Humphreys and Hatherly [1995].

$$f_v = 1 - \exp\left(-\frac{\pi}{3}\dot{N}G^3t^4\right) \quad (2.3)$$

Equation 2.3, where the extended volume fraction is transformed into the actual volume fraction by a simple exponential is used as the final calculation within the model being proposed in this work.

2.6.2 Recrystallization in Mg Alloys

Only a modest amount of work has previously been performed on static recrystallization of the AZ31 alloy. Previous recrystallization work focused primarily on recrystallization kinetics and the resulting texture. Thus far, it is known that static

recrystallization in AZ31 produced little to no texture change [Gottstein and Samman, 2005] and that significant deviations away from the ideal Avrami equation are common among many annealing temperatures and times [Su et al., 2008].

Recently, while modelling recrystallization in AZ31, Kawalla and Stolnikov [2004] applied the Avrami equation Eqn. 2.3 and by defining a series of constants they were able to model the static recrystallized fraction vs. time at high temperatures (350°C - 400°C). It is difficult however to determine the exact physical significance of these constants and thus it is difficult to determine if the model will function properly for all possible deformation routes, temperatures and times. A wider range of static recrystallization kinetics for AZ31 was investigated by Su et al. [2008]. They noticed significant deviations away from the ideal Avrami equation which they attributed to non-random nucleation sites and a varying nucleation rate.

It can thus be appreciated that while equation 2.3 provides a fair description of the recrystallization process, it still encompasses many rigid assumptions that are not appropriate for magnesium. The Avrami equation assumes constant nucleation and growth rates, a random nuclei distribution and that the incubation time is negligible. In practice, few of these are actually valid and alternate models need to be used [Humphreys and Hatherly, 1995]. Thus, a useful model must not only account for the initial condition of the material but monitor the constantly changing relationship between the growing grains and the deformed matrix while accounting for non-random nucleation sites.

A method recently suggested by Dunlop et al. [2006] can capture some of these changing relationships by coupling of previously developed models. Their model uses a nucleation criterion which monitors the effects of subgrain growth and recovery on the competition between the capillary forces opposing the growth of nuclei, and the stored energy available for recrystallization. In their studies, the model was applied

to pure cubic materials such as Cu and cubic alloys such as Al-1% Mg, predicting recrystallization kinetics with good accuracy. The model was also used by Dunlop et al. [2007] to model the recrystallization of HCP Zircaloy-4 and it had a very good fit with experimental data. The governing equation of the model is shown in equation 2.4 and the reader is directed to Dunlop et al. [2006] for a full derivation.

$$f_v = 1 - \exp \left[-\frac{\pi}{3} \int_0^t \dot{N}(t') \left(\frac{2\gamma_{se}}{G(t')} + \int_{t'}^t (M_{gb} G(t'') dt'') \right) dt' \right] \quad (2.4)$$

The model by Dunlop et al. [2006] cannot, however, be applied directly to magnesium. In all previous cases, the Dunlop et al. [2006] recrystallization model dealt with materials where recrystallization was found on grain boundaries, the stress was distributed uniformly throughout the matrix and the main mechanism of recrystallization was strain induced subgrain boundary bulging. The model has yet to be applied to magnesium and before it can be, it will need some modification in order to be applicable. Although most of the underlying recrystallization principles should be the same, the model will need to be adjusted to account for the faster recrystallization within the twinned fraction.

It is difficult to study static recrystallization for the same reasons for which it is difficult to study static recovery. These difficulties limit the amount of static recrystallization data within literature. Therefore, before a model can be fully produced and compared to recrystallization results, some dependable recrystallization kinetics must be determined.

2.7 Modelling

2.7.1 Recovery

In order to model recovery, the Verdier et al. [1998] recovery model can be used. The model presumes that the internal stress build up in a material is a result of an increase in dislocations formed during deformation. Thus, to model recovery successfully, the plastic relaxation of a material needs to be determined. During plastic relaxation, elastic strains are replaced by plastic deformation according to equation 2.5

$$\frac{d\sigma_i}{dt} = \dot{\varepsilon}_p E \quad (2.5)$$

where σ_i is the internal stress and E is the Young's modulus. Assuming further that the relaxation rate of the internal stress must occur by a thermally activated mechanism, it can be said that the internal stress decreases according to equation 2.6

$$\frac{d\sigma_i}{dt} = -K \exp\left(\frac{-U(\sigma_i)}{kT}\right) \quad (2.6)$$

where K is a constant, T is temperature and U is the activation energy. Since a material with more internal stored energy will require less external energy to activate flow, a linear relationship exists between the activation energy and amount of remaining stress according to Eqn. 2.7

$$U = U_o - \nu\sigma_i \quad (2.7)$$

where ν is the activation volume of the recovery events. Equation 2.7 allows the activation energy to decrease with an increase of internal stress. Furthermore, combining Orowan law, Eqn. 2.8

$$M\varepsilon_p = \rho b \bar{V} \quad (2.8)$$

where \bar{V} is the average dislocation speed and \mathbf{b} the Burgers vector with equations 2.5 and 2.6 the plastic strain relaxation rate $\dot{\epsilon}_p$ can be obtained

$$\dot{\epsilon}_p = \frac{\rho \mathbf{b}^2 v_d}{M} \exp\left(\frac{-U_o}{kT}\right) \sinh\left(\frac{\sigma_i \nu}{kT}\right) \quad (2.9)$$

which when substituted into equation 2.5, produces a kinetic equation for the change of internal stress

$$\frac{d\sigma_i}{dt} = \frac{64\sigma_i^2 v_d}{9M^3 \alpha^2 E} \exp\left(\frac{-U_o}{kT}\right) \sinh\left(\frac{\sigma_i \nu}{kT}\right) \quad (2.10)$$

where ρ was obtained using the forest hardening equation $\sigma = M\alpha G\mathbf{b}\sqrt{\rho}$ and $G = \frac{3E}{8}$. This kinetic equation can then be numerically fit via the Levenberg-Marquadt algorithm [Press. W., 1992] using a numerical integration based on the Runge-Kutta algorithm with U_o and ν as parameters.

2.7.2 Recrystallization

In order to model recrystallization in AZ31, a modified version of the Dunlop et al. [2006] can be utilized. The derivation of the model used by Dunlop et al. [2006] is extensive and will not be included in this literature review section. The reader is asked to refer to the reference provided for a detailed explanation of the model derivation.

The model performs well for many materials; however, for magnesium it needs to be modified in order to include some differences regarding recrystallization mentioned in the literature review. The first modification includes the addition of a new recrystallization mechanism based on subgrain growth. This modification accounts for subgrains that grow with a misorientation gradient leading to the production of HAGBs. Such growth will take place within twins as they are areas of high stored

energy and high dislocation density within AZ31. This mechanism will produce recrystallization kinetics within the twinned region of AZ31.

Modelling recrystallization in the balance of the material, the untwinned region, requires a second modification. The second modification is the assumption that the rest of the matrix will recrystallize from nuclei that form on points of intersection such as twin/twin and twin/grain boundary (GB) as these are areas of highest misorientation. Once grains nucleate on these intersections, they continue to grow and consume the remaining matrix until stored energy is exhausted.

Chapter 4 of this work deals more specifically with the derivation of equations necessary for the aforementioned modifications and discusses further implementation of the Dunlop et al. [2006] model into predicting recrystallization in magnesium.

Chapter 3

Experimental Procedure

This chapter discusses the various experimental techniques used during the entirety of this work.

3.1 Experimental

Since recovery and recrystallization are interrelated processes, in order to study them individually it is important to design experiments which suppress one and allow the other to continue unaffected. Once the kinetics of both are understood, they can then be pieced together and modeled as a single working entity. Choosing the correct experimental conditions and alloy compositions allows for this exact situation to take place.

In order to study recovery, precipitation growth was minimized by working with magnesium alloy AZ31 which is reported to have a low precipitate volume fraction. The low precipitate volume fraction was later confirmed by TEM analysis. Furthermore, recrystallization was suppressed by working at temperatures lower than 150°C below which recrystallization should not take place and this was confirmed using metallography. Once the recovery kinetics were understood, they were extrapolated to the higher temperatures during which recrystallization was studied.

3.1.1 Materials

A commercially produced AZ31 sheet supplied to McMaster by GM Corporate R&D Centre in Warren MI was used in this study. The AZ31 sheet was received in the AZ31-H24 state and was solution treated at 400°C for 24h inside an inert atmosphere in order to remove all prior stored energy and any precipitates as a precaution, even though none were expected to exist in this alloy. The AZ31 Solution Treated at 400°C for 24h (AZ31-ST) will from here on be referred to as AZ31-ST. The composition of the as received sheet is listed in Table 3.1 and was obtained through Inductive Couple Plasma (ICP) analysis after digesting samples in HCl.

Table 3.1: Material Composition Magnesium AZ31

	Al	Ca	Cr	Cu	Fe	Mn	Zn
(wt%)	3.41	0.002	0.001	0.003	0.007	0.45	0.97
STD	0.35	0.001	0.000	0.001	0.004	0.04	0.05

3.1.2 Microstructure Characterization

In order to produce an excellent microstructure, grinding was performed with SiC paper; 1200, 2400 and 4000 using water as a lubricant. Polishing then followed with a Nap cloth; 9 and 3 micron slurry using diamond ethanol based lubricant with a final polish of 0.05 colloidal silica also on NAP cloth. Final Etchant: (6g picric + 100 ml ethanol + 5 ml acetic acid + 10ml water) for 10-30sec. It is important to note that grinding using lower grit SiC may cause undesirable surface defects. No water is to be used during any of the polishing steps as it will corrode the surface and cause pitting.

3.1.3 Texture

Texture analysis was performed and pole figures were established from texture measurements performed using a Bruker X-ray diffraction goniometer. All analysis was performed along the original rolling direction with Cu K α radiation. The texture measurements were then processed through MTM-FHM software to generate both (0001) and (10 $\bar{1}$ 1) pole figures. Texture measurements were performed on samples before and after rolling.

A sample of AZ31 solution treated at 400°C for 24h then heated to 400°C for 2h to facilitate grain growth was cut into different pieces and each was rolled using a different rolling method. Some pieces were rolled along the original rolling direction, others perpendicular to it, while others had a varying rolling angle. Resulting textures were compared and reflections from each sample were studied for intensity strength changes and/or texture rotation away from the original location.

3.1.4 Recovery

To study recovery, tensile samples were prepared according to ASTM standard B557M07 from solution treated AZ31 sheets that were rolled in the original rolling direction (RD) to either $\epsilon=0.1$ or $\epsilon=0.3$ of equivalent strain according to Equation 3.1. Tensile samples were then annealed in a stirred oil bath at temperatures of 150°C or 120°C for a series of different annealing times ranging from 5 - 90 min. The low temperatures were chosen to avoid recrystallization. After the short anneal, samples were quenched in water and subject to tensile testing during which the 0.2% yield strength was recorded and plotted versus anneal time. The change in yield strength was then correlated to the change of the internal stress with annealing time and a rate of dislocation annihilation was determined. The recovery kinetics were then

analyzed using the Verdier et al. [1998] recovery model. The model presumed that the internal stress build up in a material was a result of an increase in dislocations formed during deformation. Thus, to model recovery successfully, the plastic relaxation of a material was determined via tensile testing. This kinetic data was then numerically fit via the Levenberg-Marquadt algorithm [Press. W., 1992] using numerical integration based on the Runge-Kutta algorithm with activation energy and activation volume as fitting parameters. The fitting was performed to experimental data for the relaxation of AZ31 from pre-strains of $\epsilon=0.1$ or $\epsilon=0.3$ while annealed at temperatures of either 150°C or 120°C.

In order to confirm recrystallization was not responsible for the decrease in yield strength, the grip region of the tensile samples was cut off, cold mounted, polished and analyzed under optical microscopy for the presence of recrystallized grains.

$$\epsilon = \left(\frac{2}{\sqrt{3}} \right) \ln \left(\frac{t_o}{t_f} \right) \quad (3.1)$$

3.1.5 Recrystallization

To study recrystallization, the AZ31-ST samples were first subject to a grain growth step consisting of a small rolling strain of $\epsilon=0.05$ followed by a furnace anneal at 470°C for 2h resulting in a relatively uniform grain size of roughly 70um. These large grain samples will from here on be called AZ31-ST-GG. This grain growth step was necessary in order to differentiate between existing grains and recrystallized grains during the anneal.

Furthermore, the large grain samples were rolled in the original RD direction to either $\epsilon=0.1$ or $\epsilon=0.3$ of equivalent strain according to Equation 3.1 then annealed

in a thermo quench salt bath at temperatures of 200°C, 250°C, 275°C, 300°C and times of 3.1s, 10s, 31s, 100s, 316s, 1000s, 3162s, 10000s ($10^{0.5}$, 10^1 , $10^{1.5}$, 10^2 , $10^{2.5}$, 10^3 , $10^{3.5}$, 10^4) and then quenched in water. Samples were then cold mount, polished and analyzed under optical microscopy to determine recrystallized fraction vs. time for each temperature. The recrystallized fraction was based solely on the size of the visible grains. After the grain growth was complete, all grains were large and thus any small grains less than 5 μ m that were found after the recrystallization heat treatment were assumed to be new recrystallized grains. The area fraction of grains was then calculated and converted into the recrystallized volume fraction.

Initial recrystallization nuclei were found by performing semi in-situ recrystallization experiments. Cold rolled samples were glued to a metal substrate using a thermally stable epoxy resin. The metal substrate allowed for samples to be polished and their initial microstructure analyzed via optical microscopy while providing rapid heat transfer to the samples when needed. Fiducial marks were added around areas of interest using microhardness indents and the samples were dropped into a hot salt bath for various times. Once an annealing step anneal was finished, the samples were quenched in water and rubbed gently on a 0.05 colloidal silica cloth once or twice to remove any salt residue. The samples were then re-etched and their microstructure was again recorded. They were then heated further, quenched, etched, and re-analyzed until a desired amount of total annealing time had passed.

3.1.6 Annealing

A large portion of micrographs within this work are presented for very short anneal times. Although samples are small and a salt bath is used due to its rapid heating rate, calculations using the lump-capacitance method show that within a salt bath

made from a standard thermo quench salt, a 1cm by 1cm by 0.2cm sample required approximately 2.5s to reach 90% of the desired temperature and approximately 9s to fully reach that state. Therefore, a material annealed for only 5s will not reach the desired annealing temperature. It is not until much longer times (>300s) where the heat up rate becomes insignificant and may be ignored. However, since all samples experience the same heat up rate, different samples can still be used for comparison and the conclusions regarding where nucleation starts are still valid.

For simplicity, the heat-up rate was not discussed extensively within the modelling section. In order to accommodate for this initial heat up phenomenon mathematically within the proposed model, the Verdier et al. [1998] recovery model was coupled with a lump-capacitance heat transfer calculation in order to determine the temperature of the sample at any time. This varying temperature replaced the constant temperature variable within the model and allowed the kinetics of the model to more closely resemble those seen in experimental results. This addition proved to have minor effects on kinetics and it will not be discussed further.

3.1.7 Transmission Electron Microscopy

TEM analysis was performed in order to determine if recrystallization heat treatments caused precipitation events.

The foils for TEM were prepared by punching 3mm diameter discs after grinding to around 80um thickness and then twin-jet electro polishing using a solution of 5.3 g Lithium chloride (LiCl), 11.16 g magnesium perchlorate [Mg(ClO₄)₂], 500 ml methanol and 100 ml butyl cellosolve at -50°C and 50-90 V. Microstructure analysis was conducted using the PHILIPS CM12 at McMaster University operating at 120KV.

TEM analysis was performed on the initial AZ31-ST-GG samples and compared to TEM analysis performed on samples that were recrystallized at $250^{\circ}C$ after cold rolling to $\epsilon = 0.3$. The acquired images were analyzed using *ImageJ*, a photo analysis software. The software was used to measure the average precipitate radius. Furthermore, assuming that the TEM sample was approximately 0.1 μ m in thickness, a volume fraction of the precipitate within the sample was estimated. This analysis was performed to determine the size and volume fraction of precipitates present before and after recrystallization and determine if the volume fraction changed during the heat treatment process.

Chapter 4

Results

This section describes the results of both experimental and modeling work performed. It is divided into the following subsections:

1. Transmission electron microscopy including signs of precipitation during annealing.
2. Recovery experiments and their fit to the Verdier et al, recovery model.
3. Texture
4. Recrystallization
5. ‘Semi’ in situ Recrystallization

4.1 Transmission Electron Microscopy

TEM analysis was performed with the help of Dr. Xiang Wang in order to investigate the potential influence of particles on the present recrystallization and recovery studies. Figure 4.1a and 4.1b shows the particles present before and after recrystallization. Figure 4.2a shows a large section of the pre-recrystallization heat treatment microstructure and Figure 4.2b shows its corresponding diffraction pattern. In similar fashion, Figure 4.2c shows a large section of the recrystallized microstructure and Figure 4.2d shows its corresponding diffraction pattern.

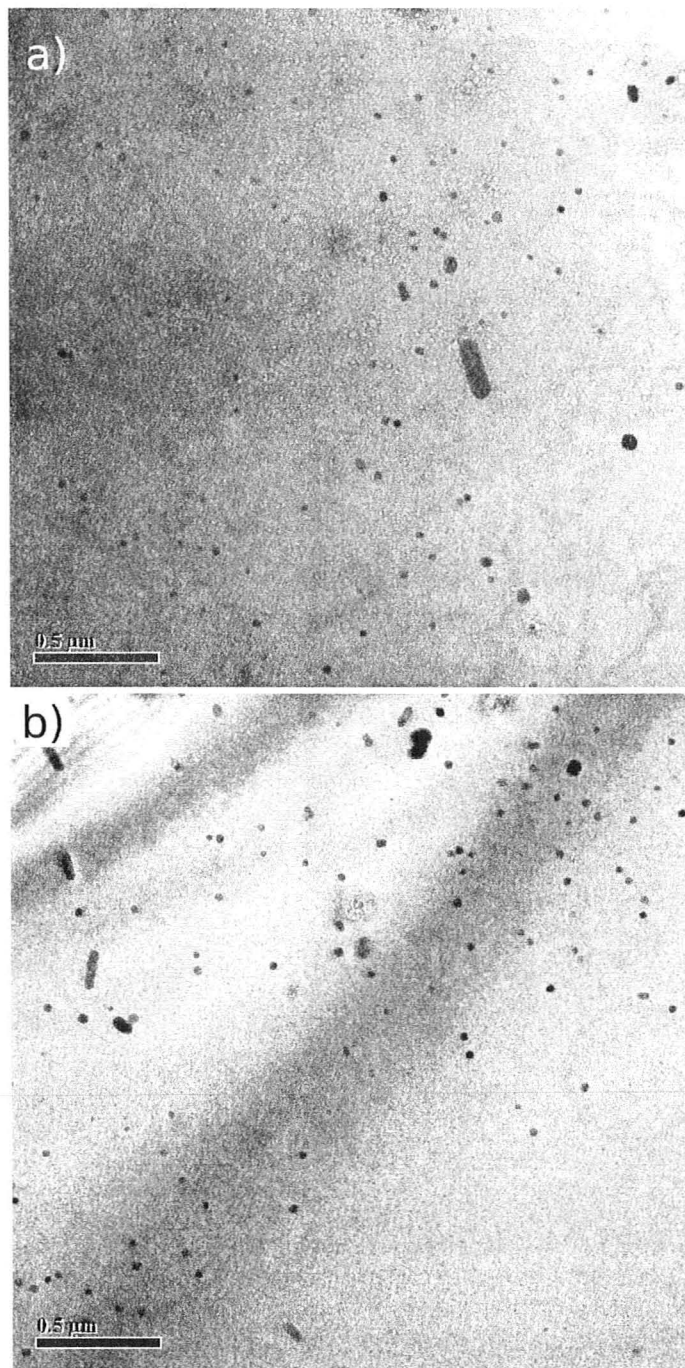


Figure 4.1: a) TEM image of AZ31-ST-GG sample showing Al_8Mn_5 distribution throughout a grain. b) TEM image of post heat treatment and deformation sample AZ31-ST-GG-CR30pct-250C-1000s showing an unchanged Al_8Mn_5 distribution throughout a grain.

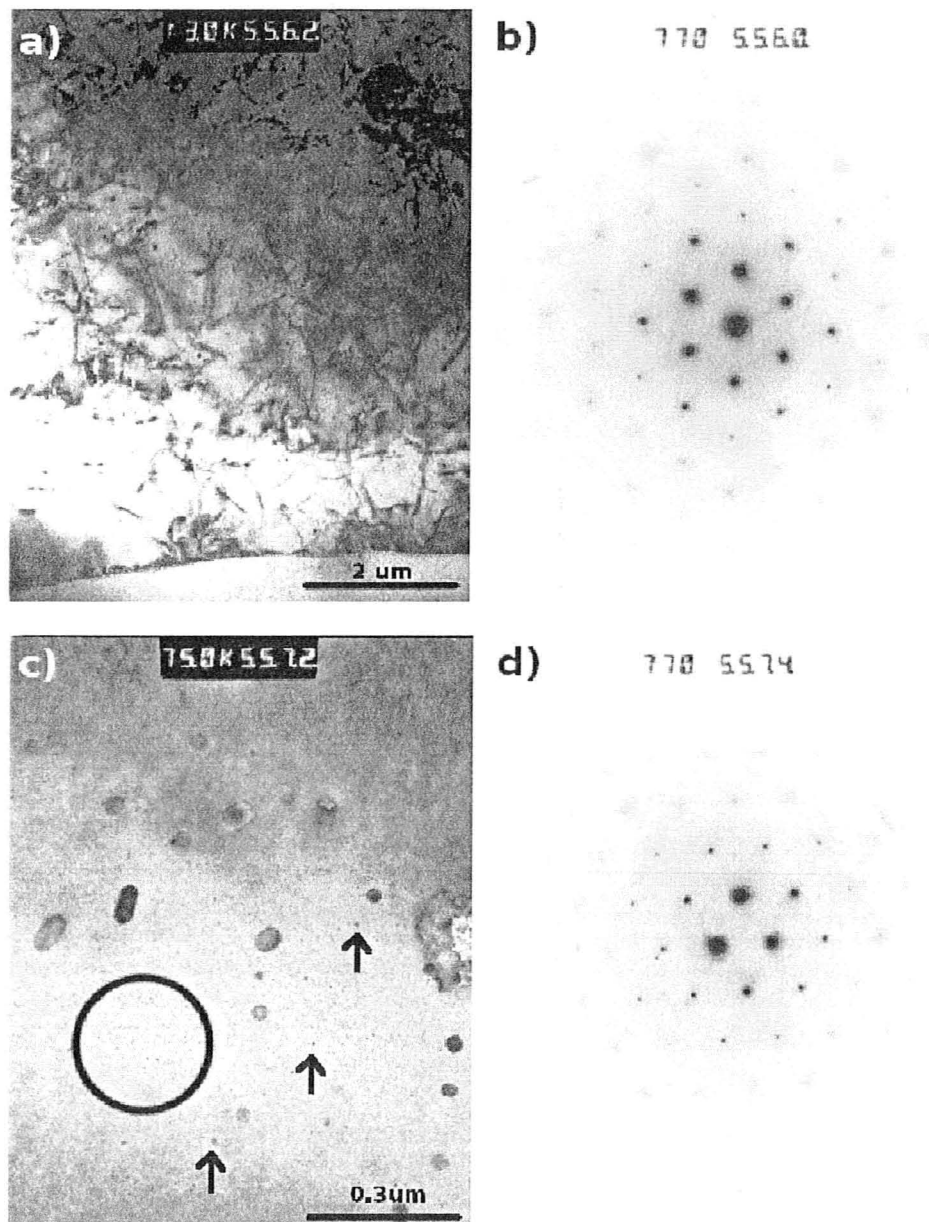


Figure 4.2: a) TEM image of AZ31-ST-GG and b) accompanying diffraction pattern. c) TEM image of AZ31-ST-GG post deformation and further heat treatment displaying signs of a small unidentified precipitate throughout the matrix. (Several instances of the new precipitate have been marked by arrows) and d) a diffraction pattern of the area highlighted in the black circle showing double reflection spots from the matrix indicating the existence of a new precipitate

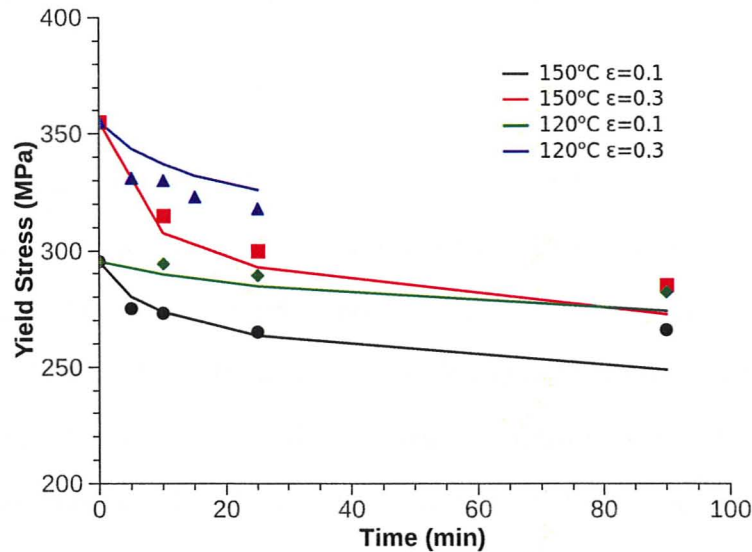


Figure 4.3: Yield Stress vs Anneal time as predicted by model (solid lines) and by experimental results (points)

4.2 Recovery Experiments and Modelling

The 0.2% yield strength versus anneal time is shown in Figure 4.3 where the points indicate experimental data and solid lines represent recovery model results which were fit using the Verdier et al. [1998] recovery model. In order to ensure that the yield strength was decreasing due to recovery and not recrystallization, optical microscopy analysis was performed and samples were inspected for the formation of new grains or grain size change. The microstructure of the recovered samples is shown in Figure 5.2.

4.3 Texture

Texture analysis was done and pole figures were constructed from texture measurements performed using a Bruker X-ray diffraction goniometer. After processing

using MTM-FHM software it was possible to generate both (0001) and (10 $\bar{1}$ 1) pole figures.

The raw x-ray intensity distribution over multiple (hkl) reflections for 3 different samples is shown in Figure 4.4. Figure 4.4a is the initial AZ31-ST-GG sample without rolling, producing a spotty intensity pattern. Figures 4.4b and 4.4c are AZ31-ST-GG samples that have been further cold rolled to $\epsilon = 0.3$ either in the b) original rolling direction or c) in the transverse direction. It is interesting to note that the intensity distribution averaged out the intensity lines for all the different (hkl) reflections producing a much finer distribution.

The intensity distribution data was further analyzed to produce corresponding pole figures for two of the most commonly reported reflections, (0001) and (10 $\bar{1}$ 1). The (0001) reflection is shown in Figure 4.5, displaying the commonly reported basal texture in the initial AZ31-ST-GG sample. The (0001) reflection recorded after varying rolling methods is shown in Figure 4.6. The texture resulting from cold rolling the initial sample in 3 different ways is shown in 4.6a, b and c where a) refers to rolling in one direction b) refers to cross rolling and c) refers to random rolling. The resulting pole figures after rolling are smoother and were averaged over the shown reflection distribution. Similar information is obtained by examining the (10 $\bar{1}$ 1) pole figure.

The first noticeable difference between initial and deformed samples was found in the x-ray reflection intensity distribution. Samples without deformation had a narrow x-ray intensity distribution when compared to the significantly larger distribution in the rolled samples (Figure 4.4). A spotty intensity distribution is found in samples with a large grain size, it is therefore expected to see the spotty intensity distribution in the undeformed samples.

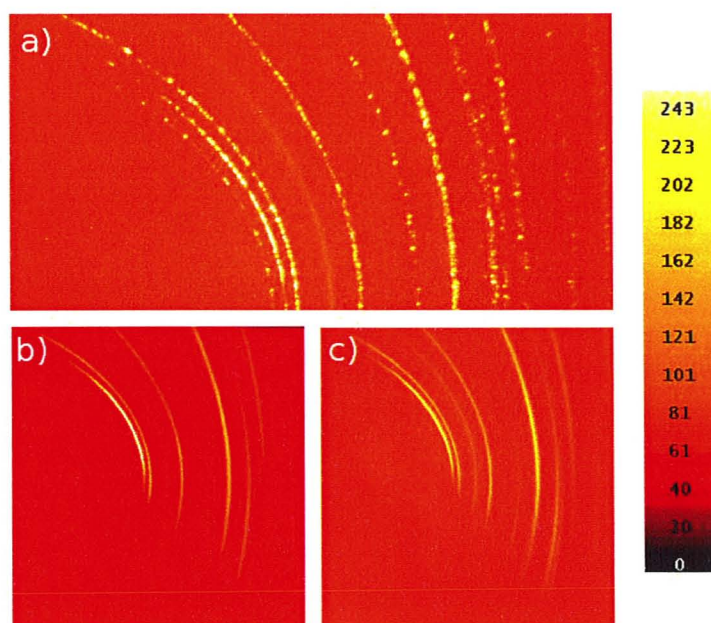


Figure 4.4: Intensity distribution of multiple (hkl) reflections taken from the raw data. a) AZ31-ST-GG b) AZ31-ST-GG further rolled parallel to rolling direction and c) AZ31-ST-GG further rolled perpendicular to rolling direction

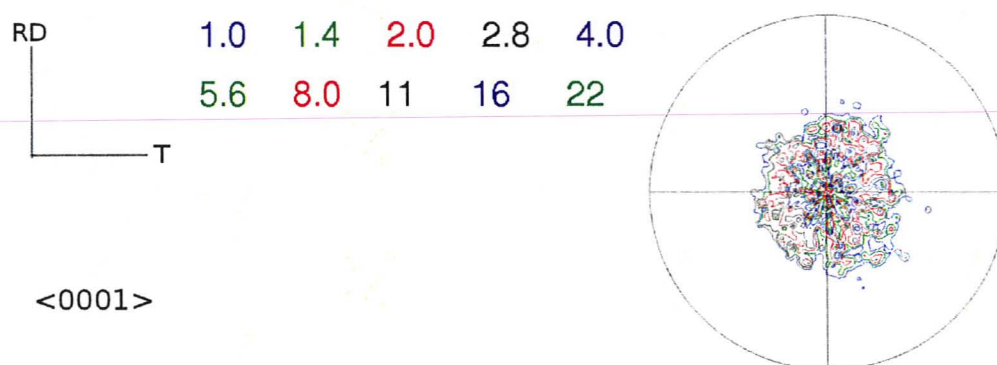


Figure 4.5: Basal plane pole figures established from texture measurements performed using a Bruker X-ray diffraction goniometer along the rolling direction with $\text{Cu K}\alpha$ radiation. The pole figure shows a solution treated (450°C for 24h) sample with grown grains ($\epsilon = 0.05$, 470°C for 2h). Numbers shown are times random.

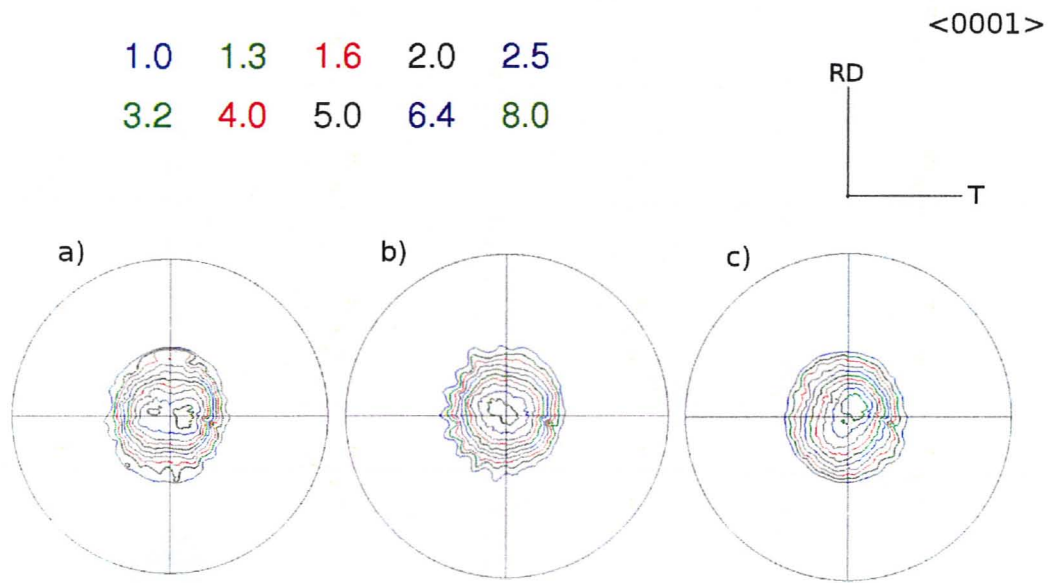


Figure 4.6: Basal plane pole figures established from texture measurements performed using a Bruker X-ray diffraction goniometer along the rolling direction with Cu $K\alpha$ radiation. Starting texture shown in Fig. 4.5: a) Rolling along original rolling direction b) Rolling perpendicular to original rolling direction c) Rolling in various ways to the rolling direction. Numbers shown are times random.

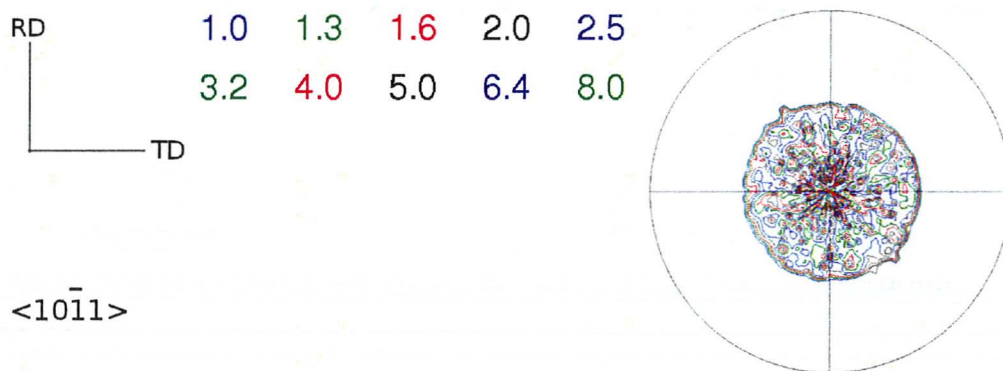


Figure 4.7: $\langle 10\bar{1}1 \rangle$ plane pole figures established from texture measurements performed using a Bruker X-ray diffraction goniometer along the rolling direction with Cu $K\alpha$ radiation. The pole figure shows a solution treated ($450^\circ C$ for 24h) sample with grown grains ($\epsilon = 0.05$, $470^\circ C$ for 2h). Numbers shown are times random.

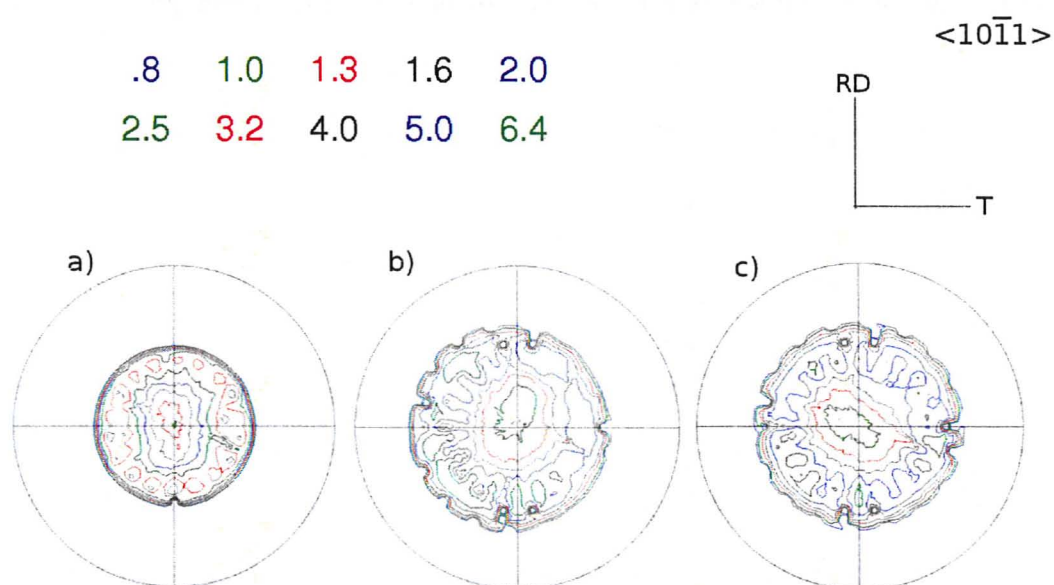


Figure 4.8: $\langle 10\bar{1}1 \rangle$ plane pole figures established from texture measurements performed using a Bruker X-ray diffraction goniometer along the rolling direction with Cu $K\alpha$ radiation. Starting texture shown in Fig. 4.7: a) Rolling along original rolling direction b) Rolling perpendicular to original rolling direction c) Rolling in various ways to the rolling direction. Numbers shown are times random.

It is possible that the changes in distribution after deformation were as a result of twinning. Twinning is highly prevalent during magnesium deformation producing a great number of twins that cut through the grains. Each time a large grain twins, it is the equivalent of producing two smaller grains. As a result of this, the average grain size decreases and the intensity distribution changes with increasing deformation. Therefore, the difference in x-ray reflection intensity distributions between the pre and post deformation samples is believed to be caused by a change in grain size due to twinning. The idea of using this phenomenon to calculate the change in grain size from twinning was entertained, however this concept was not further pursued due to time constraints.

Using reflection data, it was possible to produce various pole figures. Only those most commonly reported are presented and further analyzed. Based on what the raw intensity data foreshadowed in Figure 4.4a, it is not surprising to find the pole figures for the pre deformation sample to be rough in appearance (Figure 4.5 & Figure 4.7). The (0001) reflection is shown in Figure 4.5, displaying the commonly reported basal texture in the initial AZ31-ST-GG sample. When comparing Figure 4.5 to Figure 4.6a, b, c no significant difference can be seen between the pre deformation sample and the deformed sample. The basal plane is normal to the rolling direction regardless of the rolling technique.

Comparing Figure 4.7 to Figure 4.8a, b, c also shows no significant difference between the pre and post deformation samples on the $(10\bar{1}1)$ reflection. One thing to note is that the texture appears to be stronger in Figure 4.8a due to continuous rolling in the same direction and weaker in samples b) and c).

4.4 Recrystallization

The recrystallized volume fraction vs. time for various temperatures was calculated using optical micrographs and the results are shown in Figure 4.9. All tests were performed on AZ31-ST-GG samples deformed to equivalent cold rolling strains of either $\epsilon = 0.1$ or $\epsilon = 0.3$. Samples cold rolled in the original rolling direction are designated as (RD) in the figure. In order to determine if varying the rolling method has significant impact on recrystallization kinetics, a second set of samples was rolled using an equal ratio of both parallel and perpendicular rolling to simulate a randomly deformed sample. Such samples were designated as the alternate roll (AR) set and are designated as such in the figure. AR and RD are compared in Figure 4.9 displaying no significant differences in the recrystallized volume fraction for all temperatures except for 300°C where a significant deviation is present. Unfortunately, further work within the semi in-situ recrystallization section indicated that the recrystallization volume fraction values determined for 300°C may not be accurate as some grains that did not actually recrystallize may have been counted towards the recrystallized fraction. The subject of 300°C recrystallization data is further touched upon in the Discussion section of this thesis.

Recrystallization performed on samples cold rolled to $\epsilon = 0.3$ displayed varying levels of recrystallization completion. At long annealing times and high temperatures, the aforementioned samples reached levels of recrystallization higher than 90%. However at lower temperatures the samples plateaued at less than 20%. Samples cold rolled to $\epsilon = 0.1$ displayed the maximum amount of recrystallization of 15% at the highest temperatures tested (275°C). However, at most temperatures below 275°C , recrystallization did not proceed further than 5%. Recrystallization kinetics for samples rolled to $\epsilon = 0.1$ are presented in Figure 4.10.

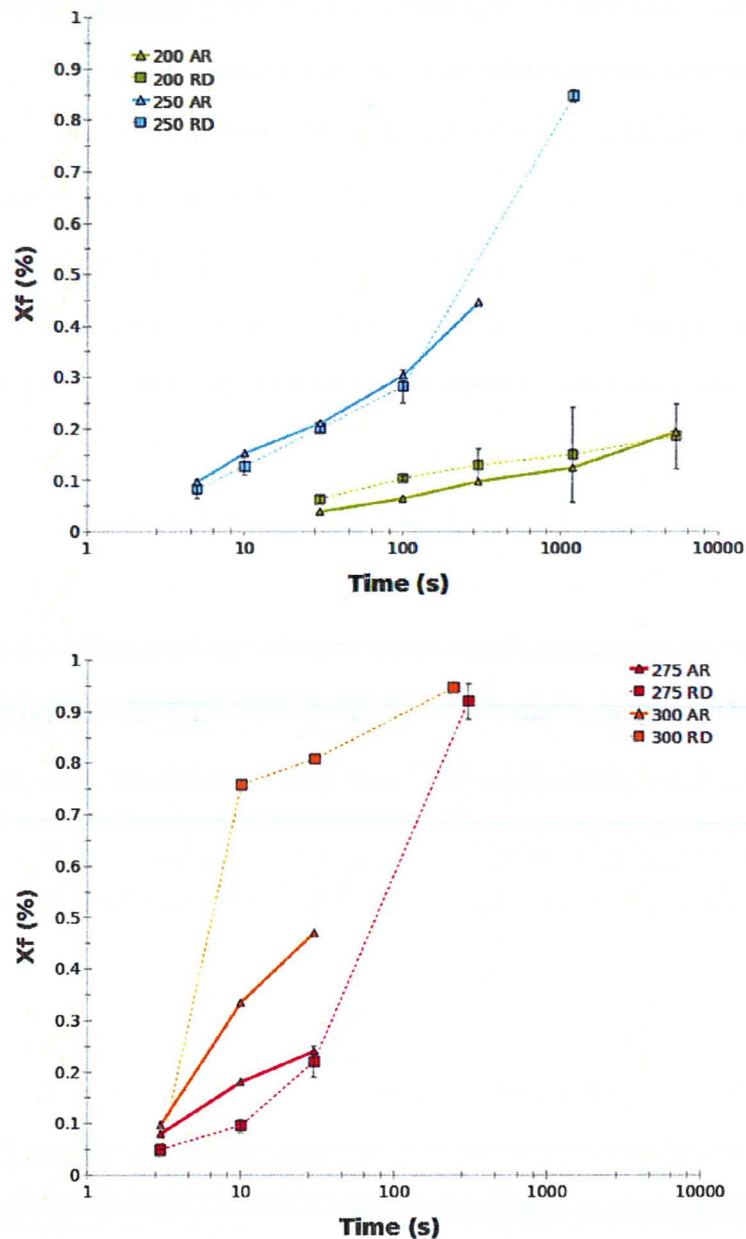


Figure 4.9: Recrystallized volume fraction at different temperatures comparing different rolling directions and their affect on recrystallization. Samples were rolled either parallel to rolling direction marked as RD, or alternated between perpendicular and parallel rolling directions marked as AD.

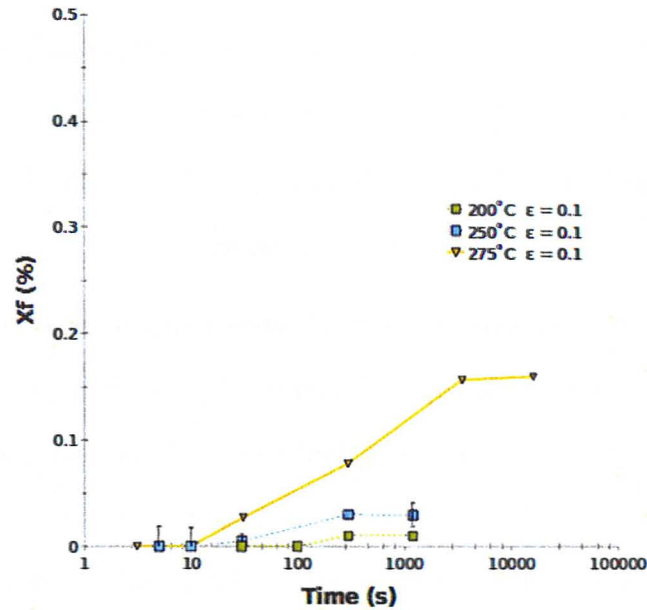


Figure 4.10: Recrystallized volume fraction with samples cold rolled to $\epsilon = 0.1$ of equivalent strain. Samples were rolled parallel to rolling direction.

4.4.1 'Semi' In Situ Recrystallization

'Semi' in situ recrystallization experiments were performed to better understand the deviation of recrystallization kinetics from the typical S-shape curves modelled by the Avrami equation. This work allowed detailed investigation of areas where recrystallization starts and how it progresses throughout the microstructure. Figure 4.11 a,b,c and d are images of the same area after various annealing times at 200°C of a AZ31-ST-GG sample deformed to $\epsilon = 0.3$ by cold rolling. This test was repeated for temperatures of 275°C and 300°C and the results are presented in Figures 4.12 a,b,c,d and 4.13 a,b,c,d respectively.

The 'semi' in situ work revealed that nucleation was most prevalent within the twinned regions of the matrix. Nuclei formed mainly within contraction twins and grains grew preferentially along the twin direction. Once nucleated within the twin volume, the twins did not appear to bulge beyond the twin boundary and remained

within the twinned volume. In order to recrystallize the balance of the matrix nuclei were forced to find other initiation sites. Recrystallization outside of the twinned region began predominantly at twin/GB intersections and twin/twin intersections and these sites have been highlighted in Figure 4.15. Nuclei at these intersections grew and consumed the adjacent matrix volume.

The ‘semi’ in situ analysis at 300°C (Figure 4.13), revealed that grains which appear to be recrystallized under optical microscopy are likely pre-existing grains which should not be counted towards in the final recrystallized fraction. Although they are pre-existing, their misleading appearance likely contributed to the previously reported high volume fraction at 300°C and produced the significant deviation seen in Figure 4.9. This finding showed that the recrystallization volume fraction vs time study at 300°C likely exaggerated the true recrystallized volume fraction. Although the recrystallization volume fraction was expected to be high at such high temperatures, the high temperature anneal process produced a partially recrystallized matrix.

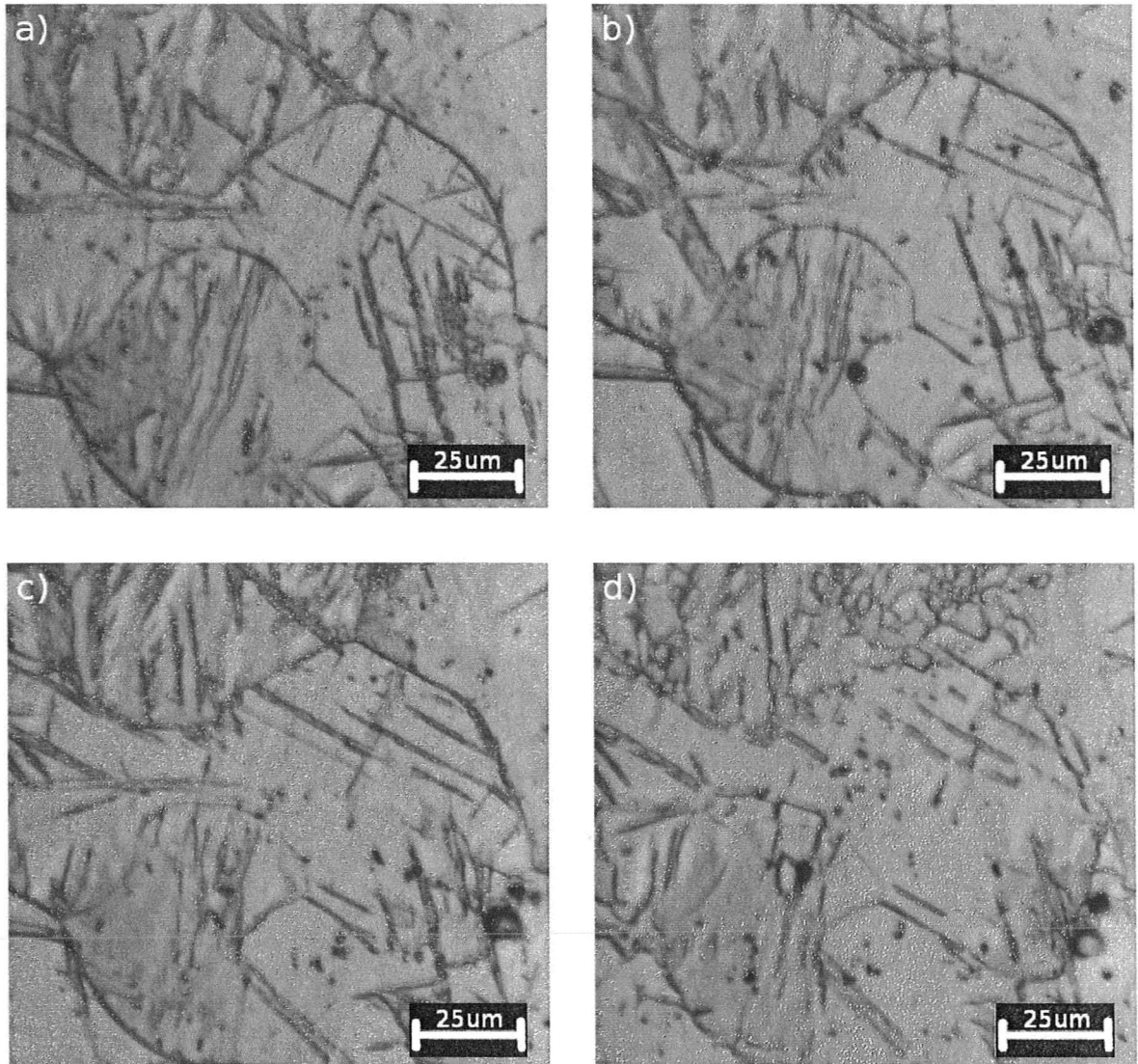


Figure 4.11: Microstructure evolution of the same area during recrystallization of 30% cold rolled AZ31 at 200°C after a) 3s of annealing b) 30s of annealing c) 100s of annealing d) 1200s of annealing

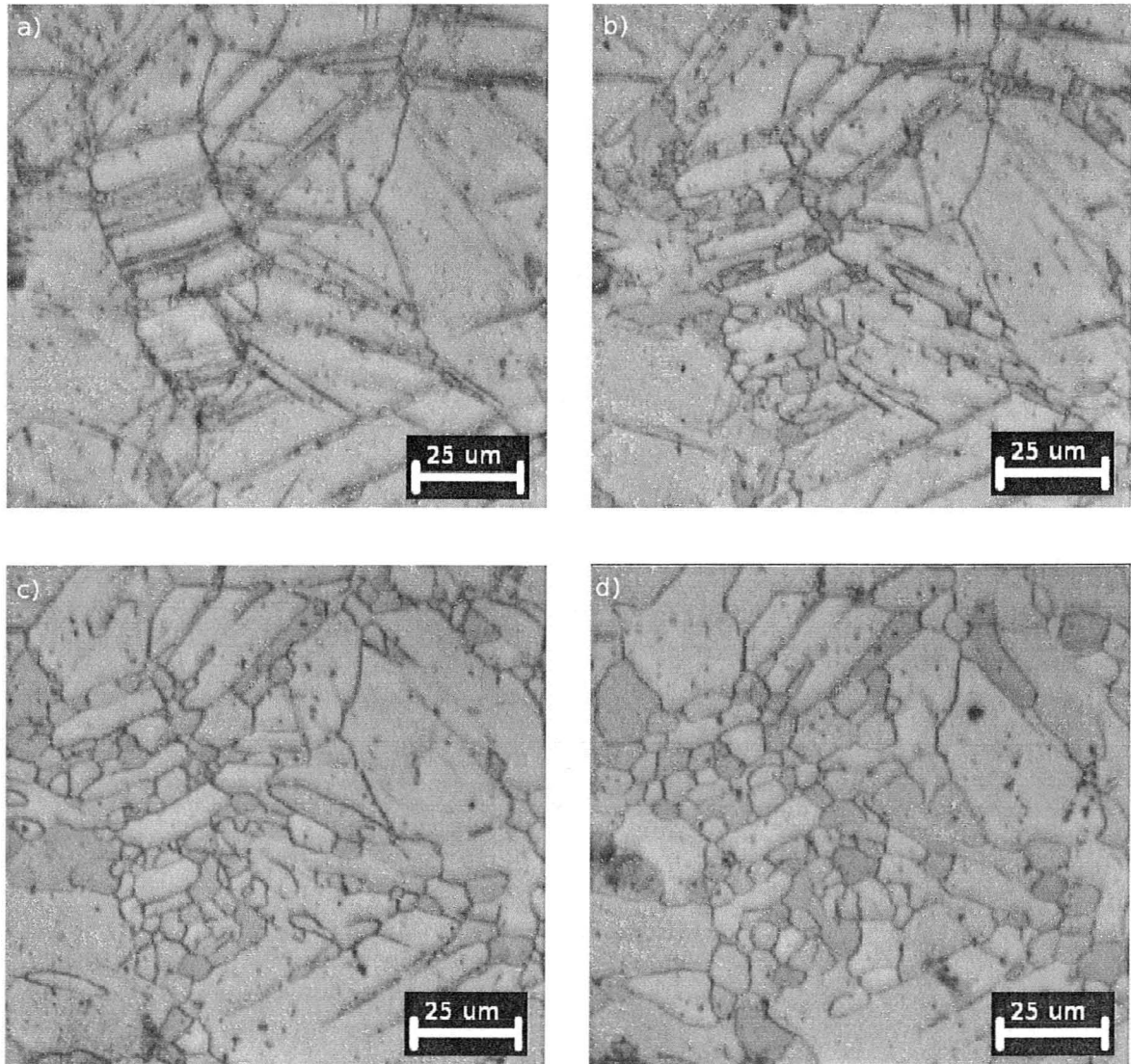


Figure 4.12: Microstructure evolution of the same area during recrystallization of 30% cold rolled AZ31 at 250°C after a) 30s of annealing b) 100s of annealing c) 300s of annealing d) 1200s of annealing

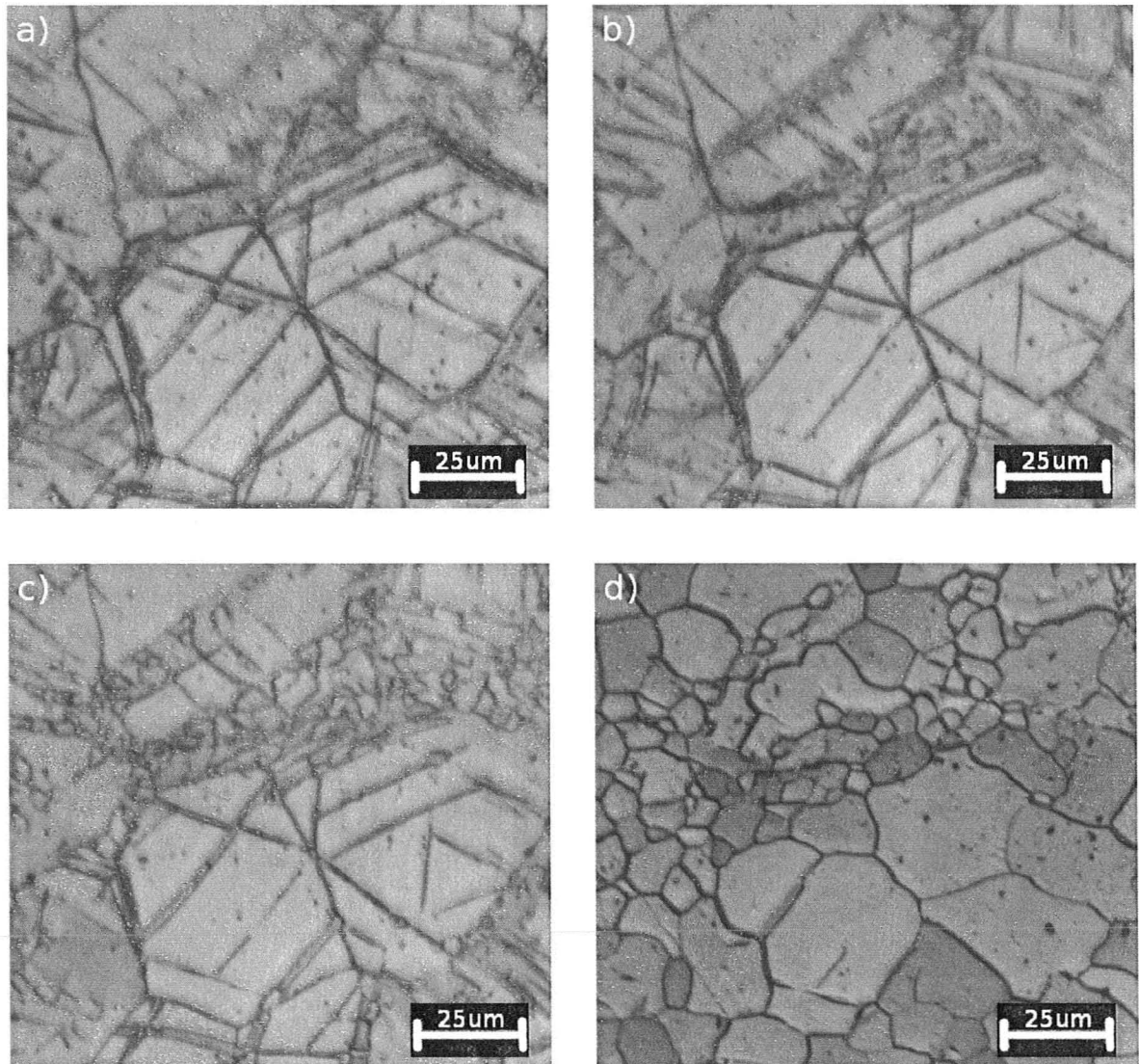


Figure 4.13: Microstructure evolution of the same area during recrystallization of 30% cold rolled AZ31 at 300°C after a) 3s of annealing b) 10s of annealing c) 30s of annealing d) 250s of annealing

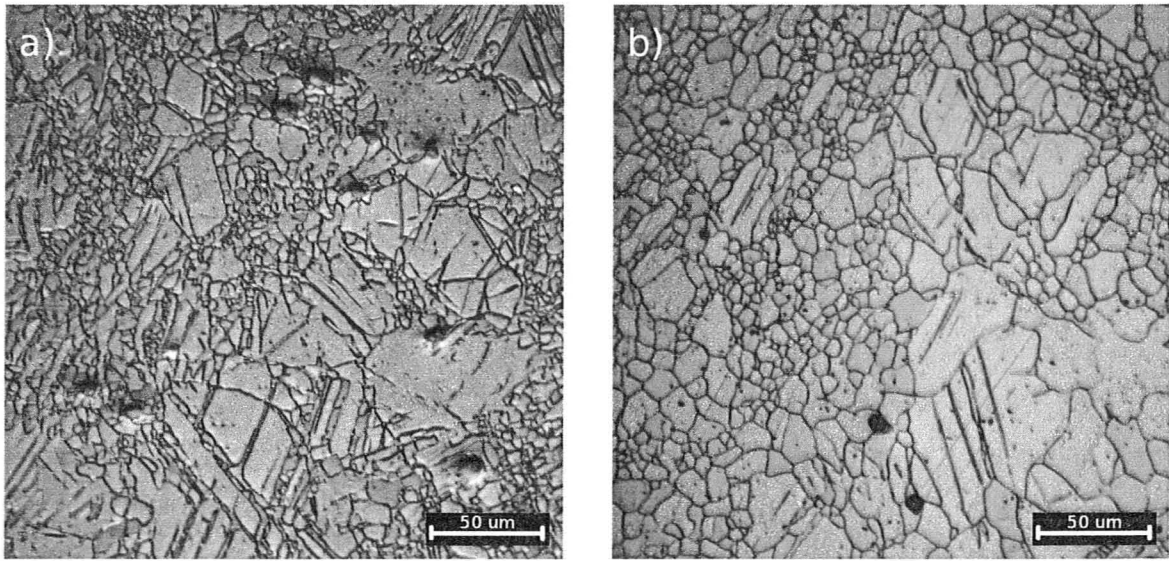


Figure 4.14: Long time annealing of 200°C sample cold rolled to $\epsilon = 0.3$ for a) 16 hours b) 48 hours

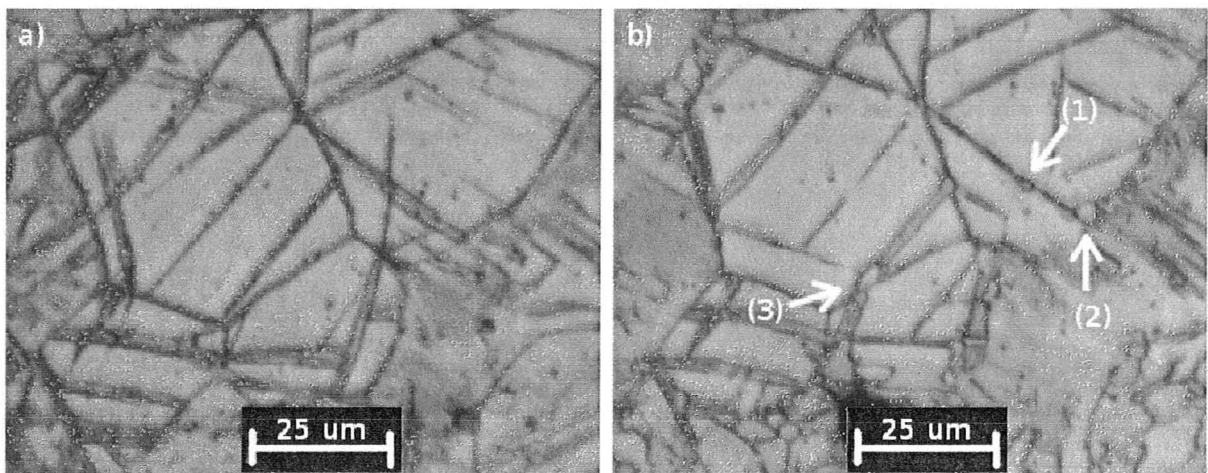


Figure 4.15: Pre anneal a) and post anneal b) images of the same area showing favourable nucleation mechanisms within a $\epsilon = 0.3$ cold rolled sample annealed at 300°C for 30s. 1) Nucleation inside twins 2) Twin/twin intersection 3) Twin/GB intersection

Chapter 5

Discussion

This chapter is meant to justify assumptions, explain experimental results and point out weaknesses. It includes reasoning for experimental methods taken during both experimentation and modeling and attempts to link the two together. Experimental results are further explained and modifications to better the recrystallization model are provided.

5.1 Transmission Electron Microscopy

TEM analysis was performed in order to understand if annealing treatments used to initiate recrystallization caused significant precipitation activity within the alloy. Precipitation events during recrystallization would likely decrease the recrystallization rate by creating an opposing force on the growing boundaries and as such, significant precipitation events would need to be accounted for within the model.

Results showed secondary phases present throughout the microstructure before recrystallization, however their frequency and size did not fluctuate during the recrystallization process. The precipitate composition was not analyzed in great detail as only the precipitate size and frequency was of importance during this TEM study. However, a literature review was performed in an attempt to identify the phases present.

The precipitates shown in Figure 4.1a and 4.1b have been identified based on morphology to be Al_8Mn_5 as they resemble in size and volume fraction those found in literature by L.Xiao et al. [2010]. Since identification by morphology is only a primary step in precipitate identification, no further comments can be made regarding the exact type of precipitates or whether multiple precipitates exist. However, since the exact type of precipitate did not play a significant role in the current model, precipitate characterization was not pursued further and remains as future work.

The volume fraction and size of the main type of precipitates present in Figure 4.1a and 4.1b are consistent throughout the recrystallization heat treatment process. As such, the Zener pinning of grain boundaries by these precipitates can be assumed constant and this value has been calculated and incorporated into the model.

The precipitate size and volume fraction as determined from TEM analysis are shown in Table 5.1. These values should not be considered definite since the TEM sample thickness was estimated during the volume fraction calculation. Although not exact, for the intended purpose, the volume fractions determined in this manner provide a reasonably accurate description of the actual values. The size and volume fraction of the present precipitates was used to determine Zener drag by Equation 5.1 as suggested by Doherty et al. [1997]. This equation relates the force (P_s) applied by the precipitate on the moving grain boundary to the precipitate's volume fraction (F_v) radius (r) and boundary energy (γ_{gb}). Table 5.1 was compiled from Figures 4.1a and 4.1b and shows that Zener drag is relatively small when compared to the driving force for recrystallization. This value was incorporated into the model by subtracting it from the stored energy available for recrystallization.

$$P_s = \frac{3F_v\gamma_{gb}}{2r}. \quad (5.1)$$

Table 5.1: Precipitation analysis in AZ31 before and after heat treatment.

Anneal Type	r (nm)	$Vf_{Al_8Mn_5}$ (%)	Zener Drag (MPa)
None	13 ± 2	0.19	0.108
$250^\circ C$ for 1000s	15 ± 3	0.22	0.106

Recrystallization samples were further analyzed in reciprocal space. Figure 4.2a shows a large section of pre recrystallization microstructure and Figure 4.2b shows its corresponding diffraction pattern. The diffraction pattern did not display any diffraction spots corresponding to precipitates and no patterns other than the typical HCP configuration were identified. By contrast, the diffraction pattern of the recrystallized sample displayed extra diffraction spots as highlighted in Figure 4.2d. This finding led to closer inspection of the microstructure at higher magnifications.

A post heat treatment microstructure at high magnification is displayed in Figure 4.2c. The figure indeed shows that a new unidentified precipitate formed during the recrystallization heat treatment. Some of the visible precipitates have been marked by arrows to help guide the eye. Again, precipitate composition was not a priority during this study; However, using the phase diagram in Figure 2.2 and morphology of the new precipitate, it is possible to speculate on its composition. The phase diagram predicts that the possible precipitate phases are $Mg_{17}Al_{12}$, Mn_4Al_{11} , $MnAl_4$ and $Mn_{23}Al_{99}$. Of those four phases, both $Mg_{17}Al_{12}$ and $Mn_{23}Al_{99}$ lose stability at the annealing temperature of $250^\circ C$ and are unlikely to be present in the recorded images. Furthermore, the small size of the precipitate indicates that it is likely composed of an element which is not in abundance. Therefore, the new precipitates are likely Mn_4Al_{11} or $MnAl_4$, or both as they are both stable at the analyzed temperatures and include elements which are scarce. Unfortunately, no further analysis was performed on the small precipitates and no definite stand can be taken.

The volume fraction of the new found precipitate is small and as such, this new found precipitate will not likely have a significant effect on grain boundary movement but will likely have a significant effect on recovery kinetics by slowing down the rate of recovery through slowing down dislocation motion. Further discussion on this subject is provided in subsequent sections. The TEM study provided insight into the precipitation events taking place during recrystallization, however to gather better statistics about precipitation, further TEM studies are recommended in the Future Work section.

5.2 Nucleation Sites

Throughout the course of this study, it was possible to distinguish regions of the matrix where nuclei of static recrystallization were most active. The semi in-situ analysis and the rapid heating used during volume fraction analysis was able to capture early nucleation sites which proved useful during the creation of the recrystallization model. Samples used to determine the recrystallization volume fraction vs. time were studied further at higher magnifications in search of early recrystallization sites. The samples of most interest were samples with a low initial deformation and short anneal times as they would slow down recrystallization and facilitate finding its beginnings.

The detailed analysis of the partially recrystallized material produced two micrographs (Figure 5.1 a and b) which are used to highlight the most active regions of recrystallization. The micrographs show that recrystallization nuclei are most active within the twinned volume, and most specifically at twin intersections. Figure 5.1 shows a cold rolled ($\epsilon = 0.1$) sample annealed a) 5s and b) 10s at $275^{\circ}C$ where recrystallization was found only within the twinned regions of the matrix. The findings

agree well with information provided in the literature review pertaining to the high stored energy within twins and support the model created during this work.

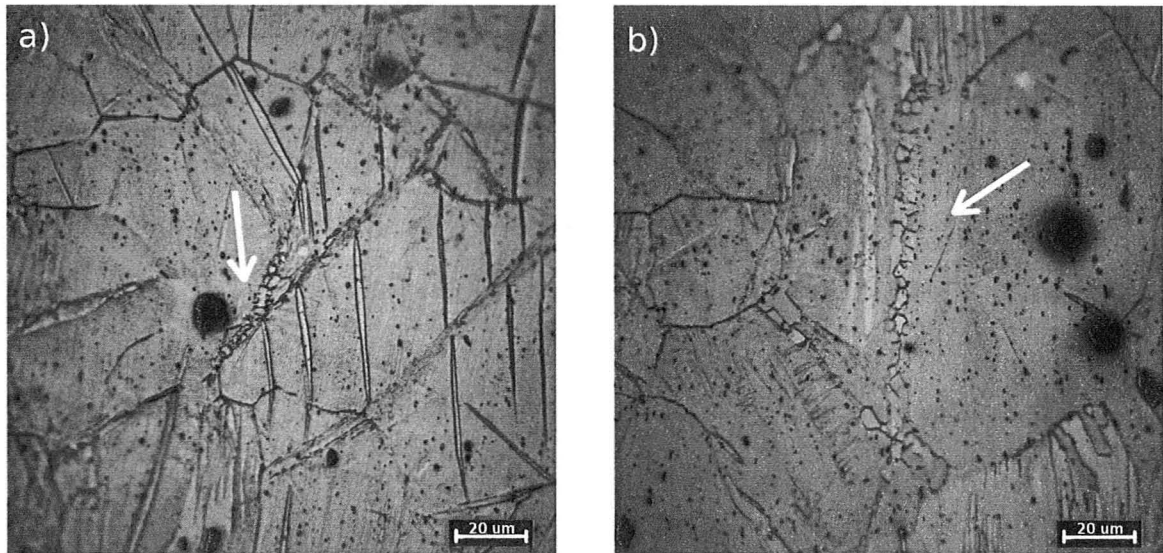


Figure 5.1: a) 5s anneal b) 10s anneal capturing the most favourable nucleation mechanisms within a $\epsilon = 0.1$ cold rolled sample annealed at 275°C

The semi in-situ recrystallization analysis was used to further understand the recrystallization kinetics as it allowed for comparison of recrystallized microstructures with their initial state. Figure 4.15a shows a sample that was cold rolled to $\epsilon = 0.3$ and Figure 4.15b shows the same region after 30s of annealing at 300°C . Some of the nucleation sites are highlighted with arrows showing 1) nucleation within a twin; 2) at a twin/grain intersection; 3) at a twin/twin intersection. Figure 4.15 further confirms that nucleation takes place initially within the twinned volume and a recrystallization model should take this into consideration.

The semi in-situ experiments help explain recrystallization kinetics by showing nuclei initiating within the twins and initial recrystallized grains consuming first the twinned fraction. As recrystallization nears completion within the twinned region, the overall recrystallized volume fraction growth slows as further nucleation and growth

in the twins is not possible. This period during which the recrystallization data has a plateau is most vividly shown in Figure 4.9 during the 200°C curve.

As annealing continues, new nucleation sites at the aforementioned intersections of twin/twin and twin/GB become utilized and recrystallization can continue to completion and consume the matrix. Although recrystallization was identified in various intersection types, the predominant place for recrystallization outside of the twinned volume was the twin/GB intersection and as such, the model uses these nucleation site exclusively to complete recrystallization of the matrix once the twinned regions are consumed.

5.3 Recovery

Throughout the recovery experiments, microstructures of samples were closely monitored to ensure no grain size effects contributed to the decreasing yield strength. Recovered samples displayed no significant changes in grain size during heat treatments and thus the yield strength decrease can be related to recovery alone.

The recovery kinetics extracted provide values of recovery activation energy and activation volume. To extract the activation energy and volume, the recovery data was fit using the Verdier et al. [1998] recovery model. The model results are presented as solid lines shown in Figure 4.3. The lines are not perfectly smooth as only the times for which experimental data exist were taken into consideration were joined by straight lines.

The activation volume and activation energy for recovery were calculated and optimized by using a root mean square method together with experimental data. The resulting parameters used in the model are shown in Table 5.2. Results show that activation energy stays constant during changes of both temperature and strain whereas

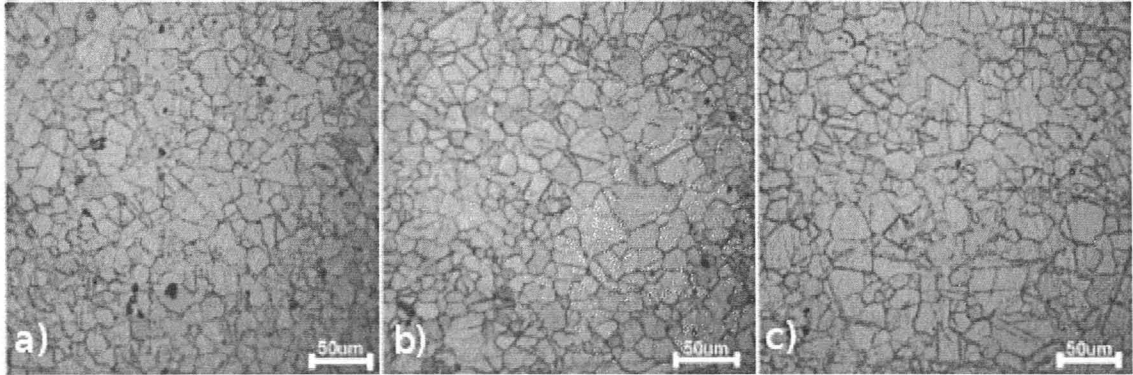


Figure 5.2: Tensile sample grip sections after a 150°C anneal for a) 0min b) 25min c) 90min showing no signs of recrystallization or any other microstructural changes throughout the recovery process

activation volume has a negative correlation with strain. The activation energy found during this study agrees well with the self diffusion of pure magnesium found in literature [Ashby, 1982]. These numbers were extrapolated to higher temperatures in order to complete the recrystallization model which relies on the recovery rate to determine recrystallization kinetics.

Table 5.2: Calculated activation energy and activation volume

$U_o(\frac{kJ}{mole})$	$V_o(b^2)$	Temp ($^{\circ}C$)	Strain ϵ
135	12	150	0.1
135	12	120	0.1
135	9	150	0.3
135	9	120	0.3

5.4 Modelling

This section will discuss and derive the proposed model used to predict recrystallization. The model will determine the recrystallized fraction of Mg based on the

literature review and the results achieved during laboratory experiments. Differences between the model and experimental results are also discussed.

5.4.1 Recrystallization

Within the proposed model, the creation of HAGBs from LAGBs can be created via the process of nucleation and growth by one of the following mechanisms:

1. Subgrain misorientation accumulation through coarsening.
2. Bulging of HAGBs.

Mechanisms 1 & 2 will now be described in more detail.

5.4.1.1 Mechanism 1

In order for sub-grains to produce HAGBs and create large dislocation-free grains, they first need to coarsen in order to accumulate enough misorientation to propagate growth. During growth and coarsening, the average sub-grain size $\langle r(t) \rangle$ reaches a critical radius $r_{c(HAGB)}$ which corresponds to a critical angle θ_c at which a LAGB becomes a HAGB. At this point, the mobility of the sub-grain boundaries increases significantly so that they can grow and consume the remaining stored energy within the matrix.

The critical radius at which the transition takes place can be determined by assuming that a gradient of misorientation $\delta = \left(\frac{\theta}{um} \right)$ exists throughout the sub-grains. As one sub-grain coarsens by a single unit of measurement, say a μm , it increases its misorientation by the value equal to the gradient. The critical radius of HAGB creation would therefore be given by:

$$r_{c(HAGB)} = \left(\frac{\theta_c - \theta_o}{\delta} \right) + r_o \quad (5.2)$$

where θ_c is the critical angle of where a LAGB becomes a HAGB (chosen to be 15°), θ_o is the initial misorientation and r_o is the initial starting radius of the subgrains.

5.4.1.2 Mechanism 2

Another method by which a material can create dislocation free grains pertains to sub-grain bulging. This mechanism is based on allowing the initially slow sub-grain boundaries to travel rapidly by using existing HAGBs and bulging into the deformed regions. In order for recrystallization to take place via this mechanism, the average sub-grain size $\langle r(t) \rangle$ must be greater than the critical radius for nucleation r_c which is based on the Bailey and Hirsch [1962] criteria and can be calculated using the following:

$$r_c(t) = \frac{2\gamma_{gb}}{G(t)} \quad (5.3)$$

It is important to note that during annealing, $G(t)$ is decreasing with time due to recovery and thus r_c is increasing over time.

5.4.2 Recrystallization in Mg Alloys

In order to model recrystallization behaviour within Mg, the model needs to take advantage of both Methods 1 & 2 in order to capture the process effectively. Experiments show that first sub-grains coarsen and recrystallize the inside of twins.

Furthermore, as twins become fully consumed, the material seeks new nucleation sites by which it can produce new grains and continue recrystallization.

This model assumes that sub-grains within the twins grow and accumulate misorientation until they either become pinned by the twin boundary and cease complete recrystallization or nuclei are formed on twin/twin or twin/GB intersections and recrystallization can continue to completion. The nuclei at the aforementioned intersections recrystallize by bulging into the matrix if the Bailey-Hirsch criteria has been satisfied. In order for the grain to bulge into the matrix, the stored energy reduction due to bulging into the matrix must be large enough to justify the energy addition of creating a new surface. Therefore, the stored energy within the matrix ($G_{matrix}(t)$) allows for the calculation of a critical grain size above which nuclei will bulge into the matrix and below which recrystallization will be limited to the twin areas only.

$$r_c(t) = \frac{2\gamma_{gb}}{G_{Matrix}(t)} \quad (5.4)$$

5.4.3 Model

5.4.3.1 Recrystallization Within Twins

The model begins by calculating the sub-grain boundary growth within the twinned area. The changing sub-grain size with time is calculated using the integral of its velocity in the following way:

$$\begin{aligned}
 v(t) &= M_1 G \\
 r(t) &= \int_0^t v(t) dt \\
 r(t) &= \int_0^t M_1 G dt \\
 r(t) &= r_o + M_1 G t
 \end{aligned} \tag{5.5}$$

The above equations determine the radius of the sub-grain boundary $r(t)$ with time by first assuming that the sub-grain boundary velocity is based on its mobility M_1 and the stored energy G where M_1 is 0.01-1 of the HAGB mobility. Assuming the velocity function of a sub-grain is known, it can be integrated with respect to time and added to an initial sub-grain size r_o in order to determine the subgrain radius $r(t)$ at any time. The initial subgrain size can be calculated since during steady state deformation, the subgrain size depends on the stress σ of deformation. The equation relating these parameters is typically of the form:

$$\frac{r_o}{b} = \frac{K}{2} \left(\frac{\mu}{\sigma} \right)^m \tag{5.6}$$

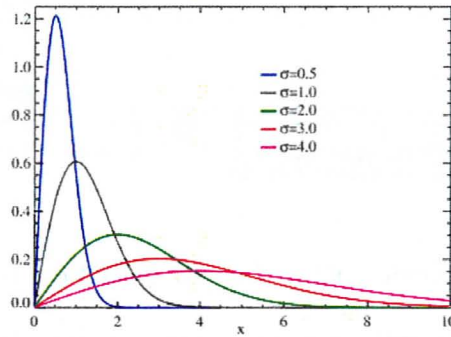


Figure 5.3: Grain size distribution based on the Rayleigh distribution function

Where r_o is the subgrain diameter, b is the burger vector, σ is the deformation stress and the values K and m are constants which can be readily found for most materials in a study performed by Raj and Pharr [1986].

At first glance, this technique seems to only take one sub-grain into consideration, however since sub-grains can be considered to be self similar*, it is not necessary to follow individual grains but it suffices to follow the average sub-grain size $\langle r(t) \rangle$ in order to predict the behavior of all sub-grains.

$$\langle r(t) \rangle = \langle r_o \rangle + \int_0^t M_1 G(t) dt \quad (5.7)$$

The average technique is sufficient, however, as different sub-grains grow, they do so at varying rates based on their starting size, misorientation and stored energy and thus at any particular time their sizes can vary. This variance in size is sufficiently described by a Rayleigh distribution which allows for the majority of grains to maintain a specific average size range while accounting for other outlier grains both at the large and small extremes. Typical Rayleigh distributions are plotted in Figure 5.3.

*Hughes et al. [1998], Hughes and Hansen [2003] measured sub-grain distributions for a variety of materials in various deformation states. Their work showed that sub-grain distributions observe self-similar scaling laws.

This distribution phenomenon is based on Louats random walk theory in which sections of the grain boundary undergo random motion leading to grain growth since grain loss by shrinkage is not reversible. The Rayleigh distribution model captures the varying sub-grain sizes and can be used to relax the strict average $\langle r(t) \rangle$ calculated by Equation 5.7. To prevent the distribution from changing with time, it is first normalized and then the normalized sub-grain size, $\chi = \left(\frac{r(t)}{\langle r(t) \rangle} \right)$ is followed as it remains invariant during the recrystallization process. The normalized Rayleigh distribution is then:

$$F(\chi) = \frac{\pi}{2} \chi e^{\left(\frac{-\pi \chi^2}{4} \right)} \quad (5.8)$$

Now that the normalized distribution of sub-grain sizes and their growth rate can be determined, it is possible to determine the fraction of sub-grains which will be larger than the critical radius necessary to produce a HAGB. As was stated earlier in the first mechanism of recrystallization, the critical radius for the creation of a HAGB can be determined by:

$$r_{c(HAGB)} = \left(\frac{\theta_c - \theta_o}{\delta} \right) + r_o$$

This criterion may also be expressed as a critical value of the normalized sub-grain size as follows:

$$\chi_{c(HAGB)} = \frac{\left(\frac{\theta_c - \theta_o}{\delta} \right) + r_o}{\langle r(t) \rangle} \quad (5.9)$$

The normalized Rayleigh distribution $F(\chi)$ can then be integrated from $\chi_{c(HAGB)}$ to a theoretical ∞ in order to determine the fraction of sub-grains which have the

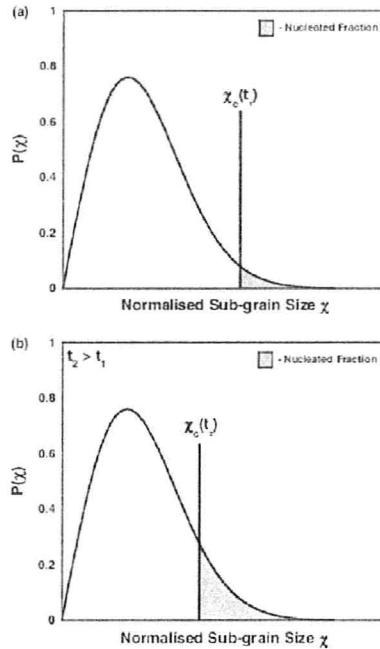


Figure 5.4: As the value of $\chi_{c(HAGB)}$ decreases with increasing annealing time a larger portion of sub-grains become HAGBs. Images (a) and (b) display the fraction of created HAGBs within the twinned region. $\sim 10\%$ in a) showing the start of recrystallisation $\sim 30\%$ in b)

potential to grow to a size large enough to become HAGBs. Since the constantly increasing $\langle r(t) \rangle$ is the denominator, $\chi_{c(HAGB)}$ constantly decreases with annealing time and the area of integration grows. Therefore, a constantly larger portion of sub-grains can become viable HAGBs sites as shown in Figure 5.4.

$$f(t) = \int_{\chi_{c(HAGB)}}^{\infty} F(\chi) d\chi \tag{5.10}$$

Once solved, the function $f(t)$ can provide the fraction of sub-grain boundaries which have the potential to grow to the point of becoming HAGBs. Before integration however, a more accurate way to describe recrystallization can be found when the integral $\int_{\chi_{c(HAGB)}}^{\infty}$ is split into the sum of $\int_{\chi_{c(HAGB)}}^3$ plus \int_3^{∞} so that integration over

the large tail seen in 5.4 can be avoided by simply ignoring or subtracting the value produced by \int_3^∞ .

$$f(t) = \exp\left(-\frac{\pi}{4}\chi_{c(HAGB)}^2\right) - \exp\left(-\frac{\pi}{4}3^2\right) \quad (5.11)$$

where $\exp\left(-\frac{\pi}{4}3^2\right)$ was subtracted to allow for integration to a reasonably high value without the need for extrapolation to ∞ .

The determined $f(t)$ can now be multiplied with the number of nucleation sites $^\dagger N$ available in order to determine the number of nucleation sites available per unit volume ($\dot{N}_{uv}(t)$) at any time:

$$\dot{N}_{uv}(t) = \frac{d}{dt}f(t)N \quad (5.13)$$

The calculation to determine the volume of recrystallized material starts by determining the volume of a recrystallized grain at time t which was nucleated at some previous time t' . This volume can be calculated by assuming the grain is spherical ‡ and replacing r from the volume of a sphere calculation with the sum of Equation 5.5 and the critical radius R_{cHAGB} at which a grain became recrystallized. The volume $V(t', t)$ then becomes:

$$V(t', t) = \frac{4\pi}{3}r^3 = \frac{4\pi}{3} \left[\left(\frac{\theta_c - \theta_o}{\delta} \right) + r_o + \int_{t'}^t M_1 G(t'') dt'' \right]^3$$

[†]The number of nucleation sites within a single twin volume can be found by assuming a unit volume of twin and dividing it by the volume of a single nuclei with a radius equal to that of the critical radius of nucleation. The number of sites N would therefore be:

$$N = \frac{1}{\left(\frac{4}{3}\pi R_c^3\right)} \quad (5.12)$$

[‡]The assumption that recrystallized grains are spherical is reasonable since recrystallized grains are equiaxed. To make the model more accurate a shape factor constant can be used in the future.

Knowing both the nucleation rate and the volume of a nucleated grain at time t' , it is finally possible to determine the extended volume fraction $\Phi(t, t')$ of grains at time t , which nucleated at time t' , by simply multiplying the number of nuclei formed at time t' by the volume $V(t', t)$ of each nucleated grain:

$$\Phi(t, t')dt = \left(\dot{N}(t')dt \right) \frac{4\pi}{3} \left[\left(\frac{\theta_c - \theta_o}{\delta} \right) + r_o + \int_{t'}^t M_1 G(t'') dt'' \right]^3 \quad (5.14)$$

In order to determine the extended volume fraction of grains created anytime between time 0 and time t both sides need to be integrated from 0 to t giving.

$$\Phi(t) = \int_0^t \left(\dot{N}(t') \right) \frac{4\pi}{3} \left[\left(\frac{\theta_c - \theta_o}{\delta} \right) + r_o + \int_{t'}^t M_1 G(t'') dt'' \right]^3 dt \quad (5.15)$$

This extended volume fraction ignores the fact that as grains nucleate they remove available nucleation area. Thus, the number of nuclei appearing in a time interval dt should over time becomes less than $\dot{N}dt$ as nuclei cannot form in parts of the specimen which have already recrystallized. The extended volume fraction therefore includes phantom nuclei (*nuclei which would have formed had appropriate space been provided*) as it calculates the volume of recrystallized sample. A way to eliminate the phantom nuclei from the equation is to use the method developed by Johnson-Mehl-Avrami-Kolmogorov typically called the JMAK equation. Equation 5.16 shows the complete JMAK equation which states that the exponential of the extended volume fraction gives an actual volume fraction of recrystallized grains f_v .

$$f_{v(HAGB)} = 1 - \exp(-\Phi(t)) \quad (5.16)$$

Substituting Equation 5.15 into 5.16, the recrystallized volume can be calculated. Unfortunately, the double integrals which results in the volume fraction calculation

prevent an easy solution. In order to solve the daunting double integral in Eqn. 5.15 it can be rewritten in the form of a Minkowski functional which converts the double integral into a series of coupled differential equations which are then numerically solvable. The extended volume fraction rewritten in the form of a Minkowski functional is then:

$$\psi_\mu(t) = \frac{8\pi}{(3-\mu)!} \int_0^t \dot{N}(t') \left[\left(\frac{\theta_c - \theta_o}{\delta} \right) + r_o + \int_{t'}^t M_1 G(t'') dt'' \right]^{3-\mu} dt' \quad (5.17)$$

The geometrical description of each order of the Minkowski functional was provided by Dunlop et al. [2007] and is reproduced in Table 5.3.

Table 5.3: Four rate equations describing the evolution of the Minkowski functionals for recrystallization and their geometrical significance

Order (μ)	Rate Equation	Geometric Significance
0	$\dot{\psi}_0(t) = \frac{8}{6}\pi \left(\frac{\theta_c - \theta_o}{\delta} + r_o \right)^3 \dot{N}(t) + M_{gb}G(t)\psi_1(t)$	Ext Vol Frac
1	$\dot{\psi}_1(t) = 4\pi \left(\frac{\theta_c - \theta_o}{\delta} + r_o \right)^2 \dot{N}(t) + M_{gb}G(t)\psi_2(t)$	Ext Surface Frac
2	$\dot{\psi}_2(t) = 8\pi \left(\frac{\theta_c - \theta_o}{\delta} + r_o \right) \dot{N}(t) + M_{gb}G(t)\psi_3(t)$	Mean Curvature
3	$\dot{\psi}_3(t) = 8\pi \dot{N}(t)$	Gaussian Curvature

After solving the Minkowski functional, it is finally possible to determine the volume fraction f_v of recrystallized grains within the twins created via the process of subgrain misorientation accumulation. These new HAGBs are dislocation free and can be considered as recrystallized grains within the twin area.

Once a sub-grain orientation is of the high angle type, its mobility (M_1) increases significantly to rates ranging anywhere between $1M_1 - 1000M_1$ [Dunlop et al., 2006].

The new grain can continue to grow according to Equation 5.7; however, M_1 is replaced by the faster M_2 and the grains grow at a higher rate. These recrystallized grains will grow throughout the twin consuming the deformed twin structure until they become pinned at the fairly immobile twin boundary. At this point, new nucleation spots need to be found in order to recrystallize the balance of the matrix.

5.4.3.2 Recrystallization Within Matrix

To recapitulate, sub-grains grow within the twinned region until they accumulate enough misorientation to become grains. These grains would prefer to grow beyond the twins, however they become pinned by the immobile twin boundaries and recrystallization ceases. Once pinned, the grains can either bulge into the surrounding matrix or simply coarsen within the twin.

The performed recrystallization experiments did not show grains bulging out of the twins and instead new grains nucleated at twin/twin and twin/GB intersections. Although it is typical of other materials to see recrystallization initiate at the grain boundaries, evidence of this behaviour was not present in this study. Nucleation was limited to twin/twin and twin/GB intersections. It is likely that the nuclei initiated at these intersections as a result of the twinning accommodation that took place once the twin was formed. As a newly created twin penetrated a grain boundary, its edge forced the adjacent grain to deform in order to accommodate the twin. These deformed regions at twin/twin and twin/GB intersections acted as ideal nucleation sites for recrystallization, more so than grain boundaries.

In order for these nuclei to become grains, they need to grow and bulge into the surrounding matrix and only do so if the following parameters are met:

The stored energy within the surrounding matrix must be large enough to overcome the capillary forces acting on the spherical grain and, the grain must possess a HAGB. It is safe to assume that all nuclei located at a twin/twin and twin/GB intersections will be within the vicinity of a HAGB and thus already satisfy the second criteria. In predicting which grains will meet both criteria, it is enough to simply look at all nuclei at these intersections and use the Bailey and Hirsch [1962] equation to determine whether they will bulge into a new grain. If this radius is not reached, only coarsening of the grains within the twins will take place and the material will not fully recrystallize. The critical radius can be found using:

$$R_{c(bulge)}(t) = \frac{2\gamma_{gb}}{G_{Matrix}(t)} \quad (5.18)$$

Where γ_{gb} is the grain boundary energy and $G_{Matrix}(t)$ is the stored energy of the matrix changing with time. The evolution of the critical radius for bulging is a result of recovery taking place within the matrix during the annealing process. Dislocations glide and annihilate one another leading to softening of the matrix and lowering of the stored energy $G_{Matrix}(t)$. The stored energy is constantly depleted because it is based on the dislocation density $\rho(t)$ as shown in Equation 5.19 which is decreasing with time due to recovery and the dislocations annihilation.

$$G_{Matrix}(t) = \frac{1}{2}\rho(t)\mu b^2 \quad (5.19)$$

As physically determining a dislocation density is highly speculative, it suffices to say that $\rho(t)$ can be related to the flow stress, σ , and the yield stress of the matrix in its fully recrystallized state, σ_y , via the forest type hardening relation:

$$\sigma(t) = \sigma_y + M\alpha_r\mu b\sqrt{\rho(t)} \quad (5.20)$$

where M is the Taylor factor and α_r is a constant. Equation 5.20 can then be rearranged to solve for $\rho(t)$:

$$\rho(t) = \left(\frac{\sigma(t) - \sigma_y}{M\alpha_r\mu b} \right)^2 \quad (5.21)$$

Furthermore, the recovery kinetics of $\sigma(t)$ can be accurately captured using a Verdier recovery model [Verdier et al., 1998] which considers recovery as a relaxation process of the internal stresses at a plastic strain rate of $\dot{\epsilon}_p$. A detailed description of $\dot{\epsilon}_p$ involving a dislocation velocity varying as a sinh function of the effective stress and including both an activation energy and activation volume was proposed by Verdier et al. [1998] and appears as follows:

$$\frac{d\sigma_i}{dt} = -\frac{64\sigma_i^2\nu_d}{9M^3\alpha_r^2E} \exp\left(\frac{-U_a}{K_bT}\right) \sinh\left(\frac{\sigma_i V_a}{K_bT}\right) \quad (5.22)$$

where U_a and V_a are activation energy and activation volume, constants ν_d and E are the Debye frequency and Young's modulus and T is temperature [§].

Equation 5.22 is able to capture the softening of σ_p with anneal time which could then be plugged into Equation 5.21 and expressed as a dislocation density. This dislocation density is then used by Equation 5.19 in order to determine how much

[§]The temperature variable T has been left as a constant within Equation 5.22 for simplicity of this derivation, however within the proposed model, it varies with time based on the heat up period. The lump-capacitance method has been adopted to solve for temperature T at any time during the initial anneal period in order to account for the sluggish heat up rate typically present in air furnace anneals. If salt or oil baths are used for heating, the heat transfer coefficient needs to be updated to represent the new heating method. Once updated, the time at which the sample reaches annealing temperature will automatically correct itself producing a more realistic model.

stored energy remains in the matrix and finally, this is the stored energy used to determine the critical radius for bulging into the matrix in Equation 5.18.

It has been shown that during annealing $G_{Matrix}(t)$ decreases, and this implies that $r_{c(bulge)}(t)$ increases with anneal time. This increase steadily requires the average sub-grain radius ($\langle r(t) \rangle$) to grow at an increasing rate in order to have a chance at surpassing the critical size. This race between $r_{c(bulge)}(t)$ and $\langle r(t) \rangle$ is shown in Figure 5.5 reproduced from Dunlop et al. [2006].

The growth of the average sub-grain $\langle r(t) \rangle$ was previously discussed and is calculated in the following way by Eqn. 5.23 which is based on the stored energy within the matrix and the mobility of the grains, similar to the growth of subgrains within the twins.

$$\langle r(t) \rangle = \langle r_o \rangle + \int_{t'}^t M_1 G(t) dt \quad (5.23)$$

Now, in order to determine the probability that grains with a normalized Rayleigh distribution bulge, the critical radius for bulging, $r_{c(bulge)}(t)$ must be converted into the critical value of the normalized grain size distribution which is:

$$\chi_{c(bulge)} = \frac{2\gamma_{gb}}{G_{Matrix}(t) \langle r(t) \rangle_{HAGB}} \quad (5.24)$$

The Rayleigh distribution can then be integrated from this critical value to ∞ in order to determine the fraction of nuclei that are able to bulge out into the matrix.

$$f_{bulge}(t) = \int_{\chi_{c(bulge)}}^{\infty} F(\chi) d\chi \quad (5.25)$$

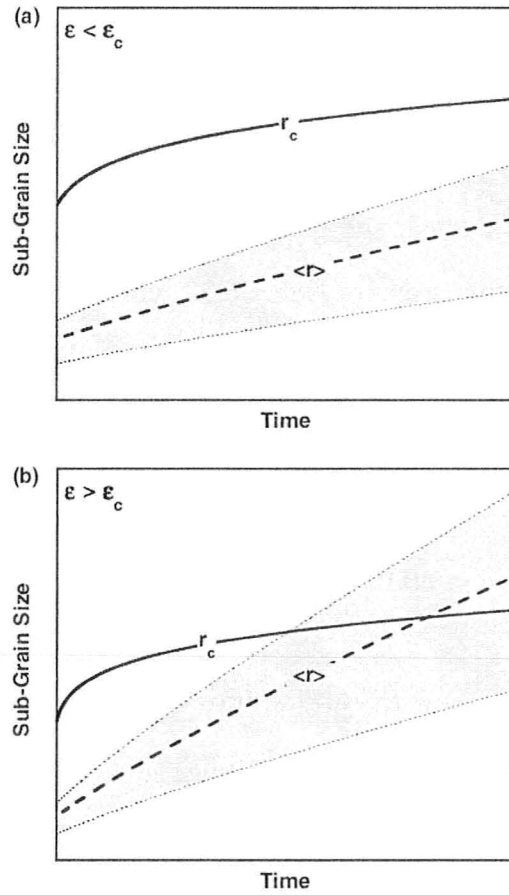


Figure 5.5: r_c changing with time. In a) r_c always grows faster than $\langle r(t) \rangle$ and no bulging happens, however in b) after a period of growth, $\langle r(t) \rangle$ overcomes and surpasses r_c allowing for bulging to take place. Reproduced from Dunlop et al. [2006]

Equation 5.25 can be split from the integral $\int_{\chi_{c(bulge)}}^{\infty}$ into the sum of $\int_{\chi_{c(bulge)}}^3$ plus \int_3^{∞} and \int_3^{∞} can be ignored so that integration over the large tail seen in Figure 5.4 can be avoided. Once solved, this fraction of subgrains can be multiplied by the number of possible nucleation sites N^{\ddagger} and produce a nucleation rate $\dot{N}(t)_{bulge} = f(t)N$, showing how many grain are bulging during any particular time dt .

To determine the total volume of material which bulged and grew into the matrix at any time t it is necessary to take into consideration all grains that bulged at time t' and the size to which they grew within the matrix at time t . This volume can be calculated by assuming the bulged nuclei is spherical and determining its radius at any given time by Equation 5.23. The volume $V_{bulge}(t', t)$ then becomes:

$$V_{bulge}(t', t) = \frac{4\pi}{3}r^3 = \frac{4\pi}{3} \left[\langle r_o \rangle + \int_{t'}^t M_2G(t)dt \right]^3$$

Knowing both the nucleation rate of bulging boundaries and the volume of all grains that bulged, it is finally possible to determine the extended volume fraction $\Phi(t, t')$ of nuclei at time t , which bulged at time t' , by simply multiplying the number of nuclei formed at time t' by the volume $V(t', t)$ of each nucleated grain.

$$\Phi_{bulge}(t, t')dt = \left(\dot{N}(t')dt \right) \frac{4\pi}{3} \left[\left(\langle r_o \rangle + \int_{t'}^t M_2G(t)dt \right) \right]^3 \quad (5.26)$$

In order to determine the extended volume fraction of nuclei that bulged anytime between time 0 and time t both sides need to be integrated from 0 to t giving.

[‡] $N = (2\pi r)tN_o$ where t is the twin thickness and r is the grain radius and N_o is the number of twins per grain. To a first approximation, each twin was assumed to traverse the whole grain. As such, the area over which the twin intersected the boundary was $(2\pi r) * t$, where the first term is the circumference of the twin. The total area of intersection per grain was crudely estimated as $(2\pi r)*t$ multiplied by the number of twins per grain N_o .

$$\Phi_{bulge}(t) = \int_0^t \left(\dot{N}(t') \right) \frac{4\pi}{3} \left[\langle r_o \rangle + \int_{t'}^t M_2 G(t) dt \right]^3 dt \quad (5.27)$$

As in the previous section, in order to solve the daunting double integral in Eqn. 5.27 it can be rewritten in the form of a Minkowski functional which converts the double integral into a series of coupled differential equations which are then numerically solvable. The extended volume fraction of bulged grains rewritten in the form of a Minkowski functional is then:

$$\psi_\mu(t) = \frac{8\pi}{(3-\mu)!} \int_t^{t'} \dot{N}(t') \left[\langle r_o \rangle + \int_{t'}^t M_2 G(t'') dt'' \right]^{3-\mu} dt' \quad (5.28)$$

The same Minkowski functional was used by Dunlop et al. [2007] during their work on Zircaloy recrystallization. The geometrical description of each order of the Minkowski functional was provided by Dunlop et al. [2007] and is reproduced in Table 5.4 similar to the previous section.

Table 5.4: Four rate equations describing the evolution of the Minkowski functionals for recrystallization and their geometrical significance

Functional Order (μ)	Rate Equation	Geometric Significance
0	$\dot{\psi}_0(t) = \pi \frac{32\gamma_{SE}^3 \dot{N}(t)}{3G(t)^3} + M_{gb}G(t)\psi_1(t)$	Ext Vol Frac
1	$\dot{\psi}_1(t) = \pi \frac{16\gamma_{SE}^2 \dot{N}(t)}{G(t)^2} + M_{gb}G(t)\psi_2(t)$	Ext Surface Frac
2	$\dot{\psi}_2(t) = \pi \frac{16\gamma_{SE} \dot{N}(t)}{G(t)} + M_{gb}G(t)\psi_3(t)$	Mean Curvature
3	$\dot{\psi}_3(t) = 8\pi \dot{N}(t)$	Gaussian Curvature

Solving the Minkowski functional calculates the extended volume fraction of recrystallized grains which can then be put into Eqn. 5.29 to determine an actual volume fraction of nuclei that bulged into the matrix $f_{v(bulge)}$:

$$f_{v(bulge)} = 1 - \exp(-\Phi(t)) \quad (5.29)$$

5.4.3.3 Total Recrystallization

It has already been described how recrystallization begins within the twins and then how it bulges into the matrix. The volume fraction of recrystallized grains within the twin $f_{v(HAGB)}$ has been solved for and the volume fraction of recrystallized matrix via bulging $f_{v(bulge)}$ has been solved for. By adding these two values appropriately, the total recrystallization within the material can be determined. It suffices to say that the total recrystallized volume fraction within the bulk material $f_{v(Tot)}$ is simply the sum of $f_{v(HAGB)}$ and $f_{v(bulge)}$ both multiplied by the amount of bulk volume they consume.

$$f_{v(Tot)} = (1 - V_{ftwin})f_{v(bulge)} + (V_{ftwin})f_{v(HAGB)} \quad (5.30)$$

5.4.4 Model Input Parameters

All variables used within the model have been summarized in Table 5.5. The table includes the value of each variable, its significance to the model and describes where the value originated.

Table 5.5: Model Input Parameters

Variable	Value	Significance	notes
V_{ftwin}	17%	Volume fraction of twins.	From this work
U_o	$135 \frac{KJ}{mol}$	Recovery activation energy	From this work
V_o	$9b^3$	Activation volume	From this work
σ_{tot}	355 MPa	Total stress	From this work
σ_{SS}	165 MPa	Solution treated stress	From this work
G_s	50 μm	Initial grain size	From this work
T_f	4 μm	Thickness of twin	From this work
θ_{twin}	5°	Initial misorientation	Estimated
$\frac{\theta}{\mu m}$	$4 \frac{deg^\circ}{\mu m}$	Misorientation Gradient	Estimated from Literature
$\frac{N_t}{grain}$	6	Twins per grain	Estimated
θ_c	15°	Critical angle for HAGB	Fixed
f	0.3 – 0.75	Mobility ratio (LAGB/HAGB)	Adjustable

Using the above parameters, it was possible to model the obtained experimental recrystallization data. Modelling results showed that the physically based model with identifiable parameters was successfully able to predict the recrystallization kinetics in AZ31. The output of the model as compared to experimental results is displayed in Figure 5.6.

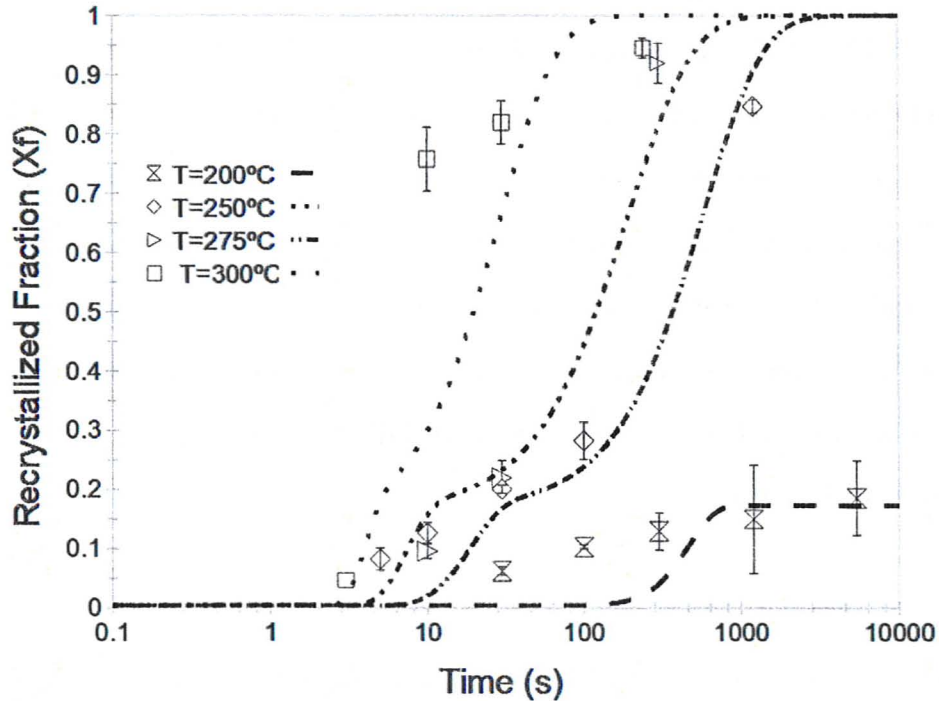


Figure 5.6: Recrystallization data compared to modelling results obtained using parameters listed in Table 5.5.

The proposed model successfully predicted experimental results of static recrystallization for various temperatures. The model predicted correctly the start and end of recrystallization and the jog visible at approximately 20% recrystallized fraction corresponds to the contraction twin fraction within the material being filled with recrystallized grains. As such, the model was able to successfully capture the initialization periods of both recrystallization within the twinned volume and recrystallization within the matrix.

The model appears to slightly overestimate and underestimate recrystallization at high and low temperatures respectively. This variation from experimental results is common across recrystallization models and is caused by averaging the stored energy during modelling. Recrystallization models average the stored energy across the

matrix, as such all regions within the matrix are modelled to recrystallized simultaneously. Physically however, not all grains are equally suited for deformation causing stored energy to be spread heterogeneously throughout the matrix. At low temperatures, the averaging effect becomes most prevalent and appears as an underestimation of the recrystallized volume fraction as pockets of higher than average stored energy recrystallize faster than predicted. At higher temperatures, active recovery can decrease the stored energy of a material and while doing so, produce regions of the matrix without sufficient energy for recrystallization leading to an overestimation of the recrystallized fraction.

The parameters listed in Table 5.5 were used to predict recrystallization at a deformation of $\epsilon = 0.3$ for various temperatures. Majority were determined from experiments performed on AZ31 during this work, however due to time constraints, several parameters were estimated based on observations and/or typical values within other materials. Although one may challenge the validity of a model containing several estimated parameters, it is important to note that sufficient statistics on twin thickness, initial misorientation, the misorientation gradient and the number of twins per grain can be obtained from a single successful EBSD study. EBSD would leave only one adjustable parameter within the model and as such, an EBSD study is a must for future work. The unknown and thus adjustable parameter within the model was the mobility of LAGBs. In order to produce a reliable and accurate value of LAGB mobility, the LAGB/HAGB mobility ratio was used as an adjustable parameter since HAGB mobility can be reasonably (*within an order of magnitude*) estimated using the Turnbull estimate, however no such relationship exists for the LAGB mobility. Following Humphreys and Hatherly [1995], it was possible to approximate the LAGB mobility by the following relationship:

$$LAGB = M(\theta)HAGB \quad (5.31)$$

where $M(\theta)$ is the distribution of sub-boundary misorientation in the vicinity of the grain boundary. This relationship was used during the calculation of the LAGB mobility within the model. The HAGB mobility was calculated using the Turnbull procedure and the ratio between LAGB/HAGB mobility was numerically adjusted to solve for the recrystallization curve which best fit the recrystallization results. The ratio was found to vary with temperature according to Table 5.6:

Table 5.6: LAGB to HAGB mobility ration at various temperatures

200°C	250°C	275°C	300°C
0.3	0.55	0.65	0.75

Table 5.6 would suggest that $M(\theta)$ is dependent on temperature. However, the distribution of sub-grain boundary misorientation should not change with annealing temperature. Therefore, another way to fit the data is to say that $M(\theta)$ is constant but HAGB mobility changes with temperature. This relationship is shown in Figure 5.7, where the ideal fit between the mobilities of $HAGB_{fit}$ and $HAGB_{Turnbull}$ should produce a linear relationship, where as fitting the values proposed within the model produces a slope greater than one. At low temperatures, the $HAGB_{fit}$ shows the greatest discrepancy against the ideal Turnbull estimate and this is likely a result of solute drag. At higher temperatures where solute drag becomes less prominent, this discrepancy decreases and the $HAGB_{fit}$ approaches the value estimated by Turnbull.

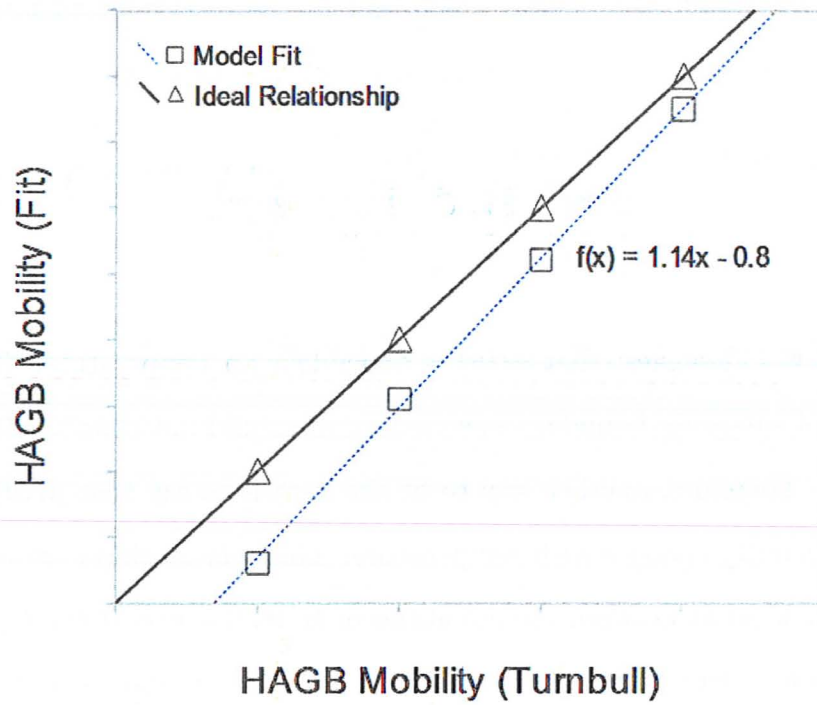


Figure 5.7: Comparison of ideal HAGB mobility as calculated by Turnbull with fitted HAGB mobility.

5.5 Model Summary

Due to the long nature of the model, a summary was created in the form of a flowchart. The flowchart has two main functions, it can be used as a summary as well as a guide while programming a computer version of this model. The flow chart spans over the next two pages and includes all of the equations used in the model. It is intended to be read downwards from the final recrystallization equation until all variable parameters are accounted for.

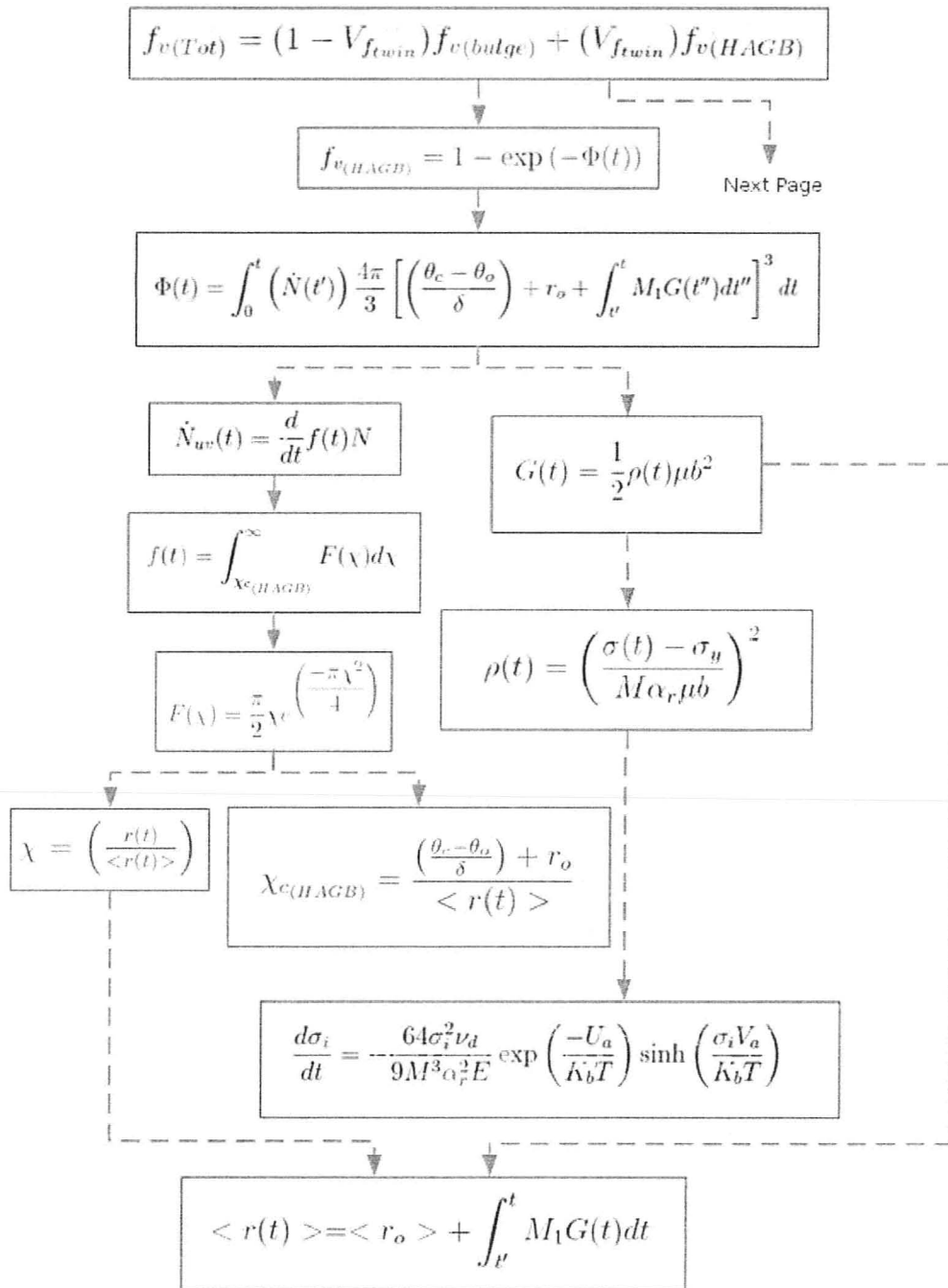


Figure 5.8: Model flowchart pertaining to recrystallization within the twin

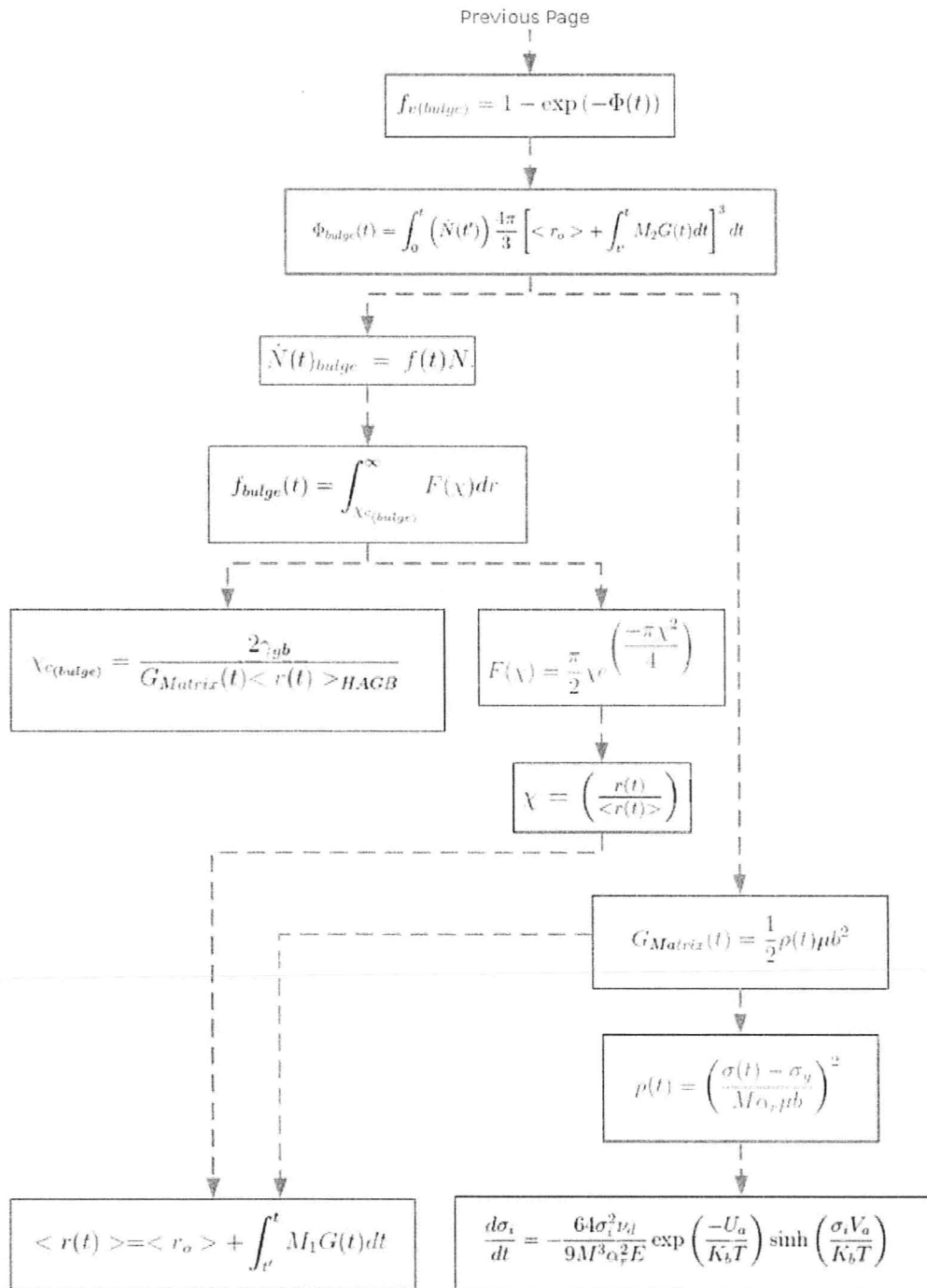


Figure 5.9: Model flowchart pertaining to recrystallization within the matrix

5.6 Model Improvements

Even though the experimental recovery kinetics were successfully fit to the Verdier et al. [1998] recovery model using reasonable values of activation energy and activation volume, these values can be further optimized by taking into consideration the effect of the precipitates found within the material after annealing as well as the grain size change due to twinning.

5.6.1 Precipitation

During the annihilation and rearrangement of dislocations, precipitates may limit the motion of dislocation segments by pinning the dislocation nodes. These segments are then unavailable to recover until coarsening of the precipitate distribution during which they become ‘unpinned’. To capture this effect, it is possible to use the method suggested by Dunlop et al. [2006] which takes a simplistic approach to the issue. Dunlop et al. [2006] modify the original Verdier et al. [1998] recovery model to account for precipitation by adding in a recovery pinning term.

$$\frac{d\sigma_i}{dt} = -\frac{64\sigma_i^2\nu_d}{9M^3\alpha_r^2E} \exp\left(\frac{-U_a}{K_bT}\right) \sinh\left(\frac{\sigma_i V_a}{K_bT}\right) \left(1 - \frac{N(t)}{N_c(t)}\right) \quad (5.32)$$

where $N(t)$ and $N_c(t)$ are the number of precipitate particles and the total number of dislocation nodes respectively. The number of precipitate particles can be experimentally determined, and the number of dislocations nodes can be approximated using the dislocation density as $\frac{1}{2}\rho(t)^{1.5}$. Once implemented, this term halts recovery when the number of precipitate particles begins to equal the total number of dislocation nodes, assuming that there is a pinning particle at each node. As annealing continues,

the particle number decreases due to coarsening, some nodes become particle free and recovery can continue.

Based on the short TEM analysis performed during this study, it is likely that adding this type of term will improve the accuracy of the predicted recovery and recrystallization kinetics so long as accurate precipitation information is first acquired. This modification would be implemented without significantly increasing the complexity of the model or adding extra adjustable parameters.

5.6.2 Grain Size

The texture results and more specifically, their raw intensity distribution shown in Figure 4.4, indicate that a significant grain size decrease takes place after rolling. To understand this size change is to consider that each deformation twin cuts the grain within which it formed into two, contributing to the decrease of the average grain size. This decrease in grain size and production of two separate grains produces new reflections, increasing the reflection intensity distribution as depicted in Figure 4.4. This grain size decrease can contribute to the increase in yield strength via the Hall-Petch effect and this contribution was not taken into account within the Verdier et al. [1998] recovery model during the stored energy calculation.

Currently, the yield strength of the material after rolling is determined via tensile testing. To iterate, the current model takes the experimentally determined yield strength and assumes that it is composed of two parts, the initial yield strength σ_y plus the contribution from the forest hardening equation, $M\alpha_r\mu b\sqrt{\rho}$. The sum of those two components is then set equal to the deformed yield strength and allows for the extraction of ρ from experimental data. However, in order to consider the

Hall-Petch effect, its contribution to the total yield strength must also be added to this sum before ρ can be extracted effectively.

The Hall-Petch effect contribution can be described as $\frac{k_y}{\sqrt{d}}$ where k_y is the strengthening coefficient, and d is the average grain diameter. The dislocation density used in the Verdier et al. [1998] model would then be calculated as follows:

$$\rho = \left(\frac{\sigma - \sigma_{ys} - \frac{k_y}{\sqrt{d}}}{M\alpha_r\mu b} \right)^2 \quad (5.33)$$

Equation 5.33 would then yield a better representation of the stored energy within the material. Since the Hall-Petch effect was not taken into consideration during this study, the true recovery kinetics may in fact be faster than reported. Since both k_y and d can be experimentally determined, this simple addition to the Verdier et al. [1998] recovery model adds no additional adjustable parameters and would produce a more magnesium focused recovery model in future versions.

5.7 Recrystallization

Temperature increased the speed of recrystallization while the rolling method had little effect on recrystallization kinetics at temperatures $200^\circ C$, $250^\circ C$ and $275^\circ C$. At those three temperatures, samples that were rolled in the original rolling direction (RD) recrystallized at the same rate as samples that were rolled in the (AD) rolling direction. At $300^\circ C$ however, the rolling technique seemed to effect the recrystallization rate and this anomalies is discussed in the subsequent section. Recrystallization curves did not follow the typical S-type recrystallization kinetics initially expected. The $200^\circ C$ curve, for example, increased very gradually until approximately 20% where it reached a plateau region, never fully recrystallizing. In order to determine

if a sample at 200°C could at one point fully recrystallize, optical metallography images were analyzed after 48h of heat treatment at 200°C . The extended annealing tests showed a slight increase in the recrystallized fraction, however unrecrystallized regions exist and a fully recrystallized structure did not form.

Curves for 250°C and 275°C both demonstrate a brief increase in recrystallized fraction at the start of annealing. This increase is sluggish and the recrystallized volume fraction grows relatively slowly. This slow growth is attributed to grains only being able to grow and nucleate within the twinned regions. After some time however, new recrystallization sites become active and the matrix can be entirely consumed completing recrystallization.

During annealing at 300°C , the rolling directions seems to have an effect on recrystallization. However, the accuracy of the values from the recrystallized fraction at 300°C is questionable as the rapid recrystallization kinetics made the distinction from the non-recrystallized to recrystallized regions very difficult via optical microscopy. It is further suggested that these values be confirmed with EBSD measurements. The fact that the RD and AD samples differed by such a large margin may be due to this measuring inaccuracy.

Since none of the curves demonstrated typical S-type recrystallization kinetics, further analysis was performed using semi in-situ recrystallization to understand the variations in the recrystallization curves.

5.7.1 ‘Semi’-in-situ Growth

The ‘semi’ in-situ recrystallization experiments were performed to further understand the shapes of the recrystallization kinetics curves. The ‘semi’ in-situ experiments could not be used to predict recrystallization kinetics as the polishing steps

likely removed a small layer of material and altered the grain appearance. However, this work proved excellent in trying to identify areas where recrystallization starts and how it progresses throughout the microstructure and was successful in capturing critical moments within the recrystallization process.

Figures 4.11 a, b, c and d are images of the same area after different anneal times at 200°C of a AZ31-ST-GG sample deformed to $\epsilon = 0.3$ by cold rolling. This set of data confirmed that recrystallization has difficulty starting at 200°C even though a significant strain was applied via cold rolling.

In order to determine if recrystallization happens at longer annealing times at this temperature, samples were left in the anneal bath for up to 2 days and still failed to fully recrystallize showing residual twins and large initial grains. The microstructure of these samples is shown in Figure 4.14 which shows samples annealed for a) 16 hours, and b) 48 hours. The long anneal times demonstrate the sluggish manner with which recrystallization takes place at lower temperatures. The sample annealed for 16 hours displays small recrystallized grains dispersed mainly within the twins. At longer times, the number of new grains stays relatively constant and instead all grains appear to have grown in order to consume more of the microstructure. Such behaviour would suggest that a critical temperature exists for nucleation within the twin/GB and twin/twin boundaries.

The same type of ‘semi’ in-situ experiment was performed at 250°C and the results are shown in Figure 4.12 a, b, c and d which are images of the same area after varying heat treatment times of a AZ31-ST-GG sample deformed to $\epsilon = 0.3$ by cold rolling. This set of data indicates that recrystallization first starts within the twinned regions and grows preferentially within the twin region. Once the twinned region is consumed, new grains can only grow once nuclei appear on areas outside of the twinned region.

At longer times, nuclei appear on twin/GB and twin/twin boundaries and lead to further recrystallization.

Finally, the ‘semi’ in-situ experiment was repeated at 300°C as shown in Figure 4.13 a, b, c and d. At this temperature, nuclei appear to form within the twinned region and along the aforementioned intersections from the start of annealing. At this temperature the critical temperature for nucleation on twin/twin and twin/GB intersections is immediately overcome. As such, the recrystallization rate is rapid.

The ‘semi’ in-situ experiments demonstrate the mechanism behind the unexpected recrystallization curves. They show that recrystallization starts within twins and continues until the twinned regions are consumed. If stored energy remains and recrystallization activation energy is overcome, nuclei begin at twin/twin and twin/GB intersections and continue recrystallization. If these intersection nuclei do not happen, such as in the 200°C example, an indefinite plateau may arise as no more material is available for recrystallization. These observations were considered during the creation of the proposed model.

5.7.2 Geometry Effects

The proposed model was primarily based on the work performed by Dunlop et al. [2006], and may be missing some fundamental aspects regarding geometry of the growing grains. The Dunlop et al. [2006] model assumes that recrystallizing grains are spheres. While nucleating at grain boundaries, the recrystallized spheres grow throughout the volume of the initial spherical matrix. The recrystallized volume (V) of a single grain has a cubic relationship to time as during the calculation of the volume of a sphere, (r) is replaced by the product of velocity (v) and time (t) giving:

$$V = \frac{4\pi}{3} (vt)^3 \quad (5.34)$$

In some situations however, the growth kinetics predicted by Equation 5.34 may realistically be too fast. These situations arise when growth is not spherical and when the distribution of grains is not random, both of which arise during magnesium recrystallization.

As reported throughout this work, the most preferred site for recrystallization nuclei within magnesium is in the twinned fraction. Therefore, new grains are not randomly distributed as assumed by Dunlop et al. [2006]. Furthermore, grains rapidly approach the thickness of the twin they are bound within and are restricted from spherical growth. Growth of a grain within a twin would best be described as two dimensional growth of a thin plate. During this growth, the time dependency would be squared since:

$$V = 2\pi (vt)^2 h \quad (5.35)$$

where h is the length of the twin multiplied by the area of a circle assumed to be the growing recrystallized grain. Eventually, the recrystallized grains within the twins lead to impingement if not enough stored energy is present within the matrix to cause bulging. Recrystallized grains begin to impinge on each other and growth in two directions becomes growth in one direction, changing the time squared dependence to a linear relationship.

Via this process, the time dependence of recrystallization may change as shown in Table 5.7.

Table 5.7: Time exponent during different types of growth

Growth Directionality	Time dependence
3-D	Cubed
2-D	Squared
1-D	Linear

This concept of a changing time dependence has been reported by the work of Cahn [1956] who extended the JMAK theory to include nucleation on grain boundaries and found that the JMAK exponent n decreased from 4 at the start of the transformation to 1 at the end.

A large factor determining the growth directionality and thus the time dependence is the location of the initial recrystallization nuclei. This phenomena can be demonstrated with a simple thought experiment displayed in Figure 5.10.

Figure 5.10 shows a schematic of two recrystallizing microstructures. On the left, nuclei are forced to start growth within the shaded region, whereas on the right nuclei can grow anywhere within the matrix. After a short incubation time, the grains begin to grow at equal rates slowly consuming the area around them. It becomes clear by step c, that the non-recrystallized area is larger in the non-random distribution since grain impingement takes place during growth. Figure 5.10 demonstrates how an initially spherical grain growing in all directions can experience impingement and continue growth in only one direction. The shaded region in this figure can be taken as the twin fraction and can be directly related to the recrystallization mechanism present in magnesium.

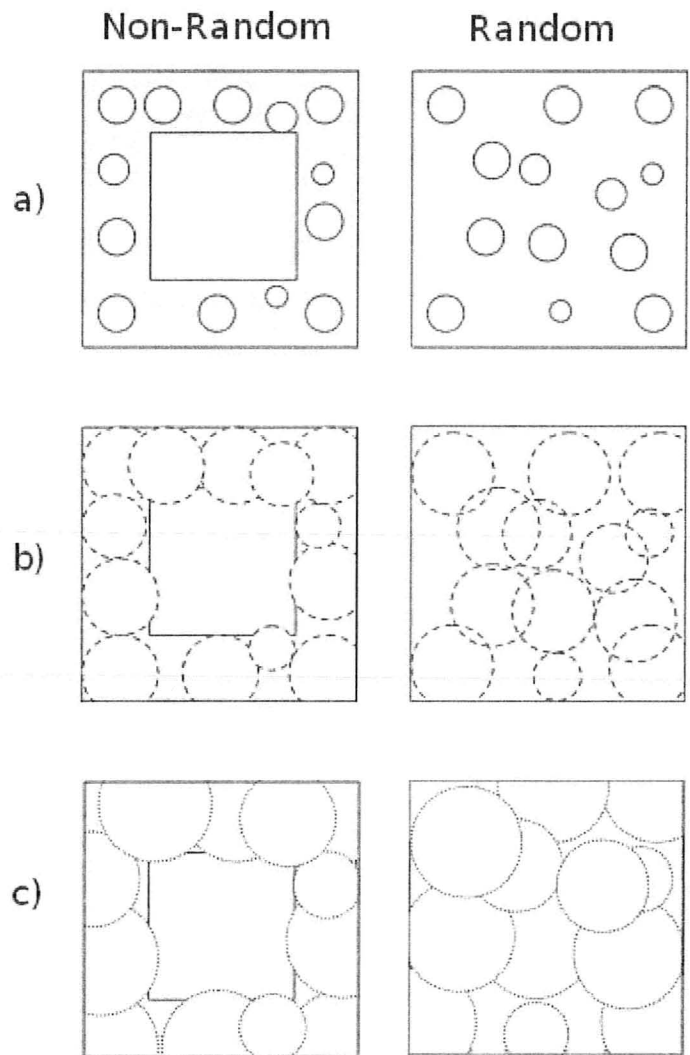


Figure 5.10: Comparison between random and non-random distribution of nuclei

5.7.3 Geometry Effects in Studied Samples

It is possible to see growth in preferential directions within the microstructures acquired during the 'semi' in-situ experiments. To show this, microstructures at higher magnifications are presented. Analysis of these microstructures successfully isolated multiple examples of grains that grew faster in certain directions (Figure 5.11). Figure 5.11a shows the initial microstructure displaying an intersection of twins which later lead to preferential growth as shown by the white arrows in Figure 5.11b, c and d. Figure 5.11d shows the final microstructure after 1200s of annealing at 250°C and the final shape of a recrystallized grain that began at the intersection of several twins. The grain grew preferentially in the direction of the twin away from the intersection point. The white arrows show that a prediction can be made regarding the way a nuclei will grow if it starts within a twin intersection. Figure 5.11 c, and d show the new recrystallized grain following the predicted growth direction and the length of the twin within which it formed.

Therefore, due to the nature of recrystallization within magnesium, a changing time dependence should be implemented into the recrystallization model in future versions. The effect of the changing time dependence is currently captured by the adjustable parameter, however if experiments suggest that this parameter can be further optimized then work on recrystallization should not stop until a changing time dependence is implemented. The proposed model is based on all observations discussed and is presented in the subsequent section.

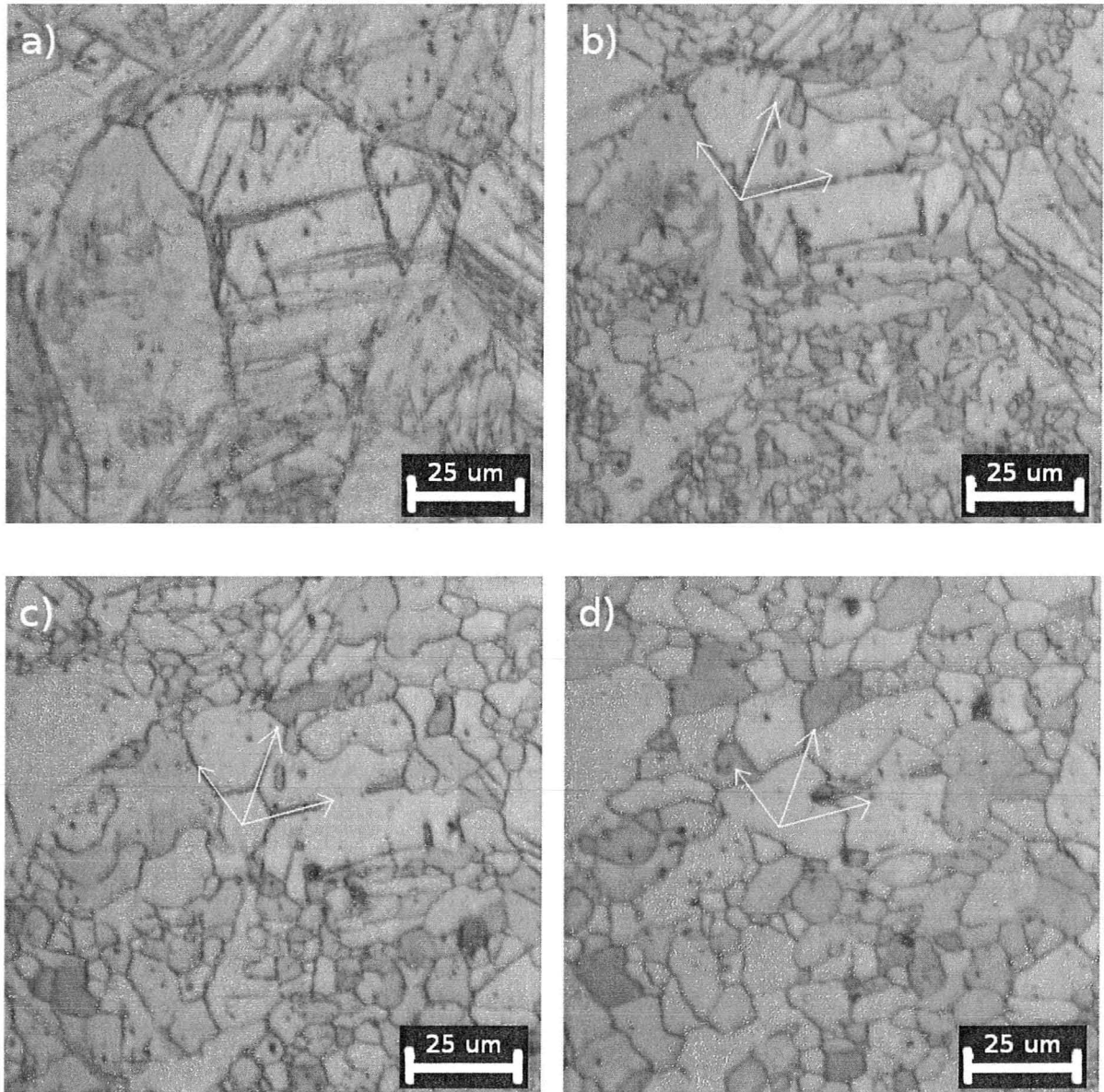


Figure 5.11: Microstructure evolution of the same area during recrystallization of 30% cold rolled AZ31 at 250°C after a) 3s of annealing b) 100s of annealing c) 300s of annealing d) 1200s of annealing. The direction lines on b) c) and d) show the predicted grain growth directions based on the initial twin intersection where a nuclei formed.

Chapter 6

Conclusions and Future Work

6.1 Conclusions

Based on the recrystallization, recovery and modelling work performed in this thesis, the following conclusions and observations are possible:

1. Recovery effects were shown to take place in magnesium AZ31 after short anneal times at low temperatures. The recovery effects were shown experimentally by following the decrease of yield strength during time of anneal and recovery kinetics were determined. Recovery kinetics were modelled successfully using the Verdier recovery model while activation energy and volume were extracted using numerical integration based on the Runge-Kutta algorithm;
2. Recrystallization nuclei within magnesium were shown to favour contraction twins as primary regions of initiation. Once contraction twins were fully recrystallized, recrystallization at lower temperatures stopped and did not complete. At higher temperatures, nucleation continued to take place at twin/twin and twin/GB intersections and allowed for the complete recrystallization of the matrix. Recrystallized grains were shown to grow favourably in the twin direction, swaying away from the typically assumed three dimensional growth kinetics;
3. Recrystallization kinetics were successfully obtained and are presented for various deformation strains and annealing temperatures. The kinetics of recrystal-

lized fraction vs time were successfully modelled by a modified version of the Dunlop et al. [2006] model. The model took into consideration experimental results and physically identifiable parameters and as such was able to follow closely the recrystallization kinetics, and;

4. The recovery and recrystallization models produced in this work are suitable for predicting the strength of structural AZ31 alloys after a given amount of deformation and annealing.

6.2 Future Work

In order to enhance and further support the proposed model, experimental work including an indepth EBSD and TEM study of AZ31 pre and post recrystallization are recommended.

Pre-recrystallization studies using EBSD can provide statistically sound and accurate values of twin fraction, initial misorientation and twin thickness. These values would enhance the model by supporting the estimates made for some of the current model parameters.

A TEM study would provide insight into the precipitation effects present in AZ31 during and after recrystallization. A more indepth TEM analysis would provide better statistics on precipitate morphology and can determine the precise type of precipitate present. Armed with better understanding of the active precipitates, a future model can account for precipitation morphology classifying it as coherent or incoherent, large or small and abundant or scarce. Understanding the nature of precipitates would allow the model to better capture the effects of precipitation on recovery and recovery on recrystallization.

Future versions of the model should account for the Hall-Petch effect while modelling recovery. Implementation of the Hall-Petch effect would produce more accurate solutions to recovery volume and activation energy and lead to a more accurate recrystallization model.

Once an accurate model exists and has been further refined by the proposed experimental results, the model can be used to produce recrystallization-time-temperature (gmail.comRTT) maps as well as predict material grain size and strength after an annealing period. Such information would be valuable to those studying formability in Mg alloys for use as a structural material.

Although a significant amount of work was performed during this study, an even larger portion was left for future eager minds to decipher.

Bibliography

- S. R. Agnew, M. H. Yoo, and C. N. Tomé. Application of texture simulation to understanding mechanical behavior of mg and solid solution alloys containing li or y. *Acta Materialia*, 49(20):4277–4289, 2001. ISSN 1359-6454.
- T. Al-Samman and G. Gottstein. Room temperature formability of a magnesium az31 alloy: Examining the role of texture on the deformation mechanisms. *Materials Science and Engineering: A*, 488(1-2):406–414, 2008.
- H.J. Frost and M.F. Ashby. *Deformation-mechanism maps*. Oxford, 1982. ISBN 0080293387.
- J.E. Bailey and P.B. Hirsch. The recrystallization process in some polycrystalline metals. *Proceedings of the Royal Society of London*, A267(1328):11–30, April 1962.
- M.R. Barnett, M.D. Nave, and C.J. Bettles. Deformation microstructures and textures of some cold rolled mg alloys. *Materials Science and Engineering*, 386:205–211, 2004.
- M.R. Barnett, Z. Kesavarz, and M.D. Nave. Microstructural features of rolled mg-3al-1zn. *Metallurgical and Materials Transactions A*, 36A:1697–1704, 2005.
- A. G. Beer and M. R. Barnett. Microstructural development during hot working of mg-3al-1zn. *Metallurgical and Materials Transactions A*, 38(8):1856–1867, 2007.
- Colleen J. Bettles and Mark A. Gibson. Current wrought magnesium alloys: Strengths and weaknesses. *JOM*, 57:46–49, 2005.

D. Bhattacharyya, E.K. Cerreta, R. McCabe, M. Niewczas, G.T. Gray III, A. Misra, and C.N. Tome. Origin of dislocations within tensile and compressive twins in pure textured zr. *Acta Materialia*, 57:305–315, 2009.

John W. Cahn. The kinetics of grain boundary nucleated reactions. *Acta Met*, 4: 449–459, 1956.

Gov Canada. Lightweight materials industry, 2002.

L. Chabbi, W. Lehnert, and R. Kawalla. *Magnesium Alloys and their Applications*. Wiley, 2001.

J.W. Christian. Deformation twinning. *Progress in Materials Science*, 39(1-2):1–157, 1995.

Frank Czerwinski. *Magnesium Injection Molding*. Springer, Dec 7 2007. ISBN 0387723994.

J.R. Davis. *Alloying: Understand the basics*. ASM International, 1 edition, 2001. ISBN 0871707446.

R. D. Doherty, D. A. Hughes, F. J. Humphreys, J. J. Jonas, D. Juul Jensen, M. E. Kassner, W. E. King, T. R. McNelley, H. J. McQueen, and A. D. Rollett. Current issues in recrystallization: a review. *Materials Science and Engineering A*, 238(2): 219–274, 1997.

M.R. Drury and F.J. Humphreys. Large strain deformation studies using polycrystalline magnesium as a rock analogue. *Physics of the Earth and Planetary*, 40: 208–222, 1985.

- J. Dunlop, H.S. Zurob, and Y. Brechet. Quantitative criterion for recrystallization nucleation in single-phase alloys: Prediction of critical strains and incubation times. *Acta Materialia*, 54:3983–3990, 2006.
- J. Dunlop, Y. Brechet, L Legras., and H.S. Zurob. Modelling isothermal and non-isothermal recrystallisation kinetics: Application to zircaloy-4. *Journal of Nuclear Materials*, 366:178–186, 2007.
- G Gottstein and T Al Samman. Texture development in pure mg and mg alloy az31. *Materials Science Forum*, 495-497:623–632, 2005.
- W. H. Hartt and R. E. Reed-Hill. Internal deformation and fracture of second-order 1011-1012 twins in magnesium. *Transactions of the Metallurgical Society of AIME*, 242:1127–1133, 1968.
- Fumiaki Hiura. Master’s thesis, McMaster, 2010.
- D. Hughes and N. Hansen. *Phil. Mag.*, 83:3871, 2003.
- D. Hughes, D.C. Chrzan, C. Liu, and N. Hansen. *Phys. Rev. Lett.*, 81(21):4664, 1998.
- F.J Humphreys and M. Hatherly. *Recrystallization and Related Annealing Phenomena*. Pergamon, 1995. ISBN 0080418848.
- A. Jäger, P. Lukác, V. Gärtnerová, J. Bohlen, and K.U. Kainer. Tensile properties of hot rolled az31 mg alloy sheets at elevated temperatures. *Journal of Alloys and Compounds*, 378:184–187, 2004.
- Jayant Jain. Phd thesis. UBC, Canada, 2010.
- R. Kawalla and A. Stolnikov. Deformation behaviour and microstructure development of magnesium az 31 alloy during hot and semi-hot deformation. *Advanced Engineering Materials*, 6(7):525–529, 2004.

- W Kelley and W.F. Jr Hosford. *Transactions of the Metallurgical Society of AIME*, 242:654–661, 1968.
- X. Li, P. Yang, L.-N. Wang, L. Meng, and F. Cui. Orientational analysis of static recrystallization at compression twins in a magnesium alloy az31. *Materials Science and Engineering: A*, 517(1-2):160–169, 2009. ISSN 0921-5093. doi: DOI: 10.1016/j.msea.2009.03.045.
- L.Xiao, L.Liu, Y.Zhou, and S.Esmaeili. Resistance-spot-welded az31 mg: Part 1. dependence of fusion zone microstructures on 2nd phase particles. *Metallurgical and Materials Transactions A*, 41A:1511–1522, June 2010.
- M. M. Myshlyaev, H. J. McQueen, A. Mwembela, and E. Konopleva. Twinning, dynamic recovery and recrystallization in hot worked mg-al-zn alloy. *Materials Science and Engineering A*, 337(1-2):121–133, 2002. ISSN 0921-5093.
- E. Nes. Recovery revisited. *Acta Materialia*, 43(6):2189–2207, 1995.
- H Press. W. *Numerical Recipes in C: the Art of Scientific Computing, 2nd ed.* Cambridge University Press, 1992.
- S.V. Raj and G.M. Pharr. *Materials Science and Engineering*, 81:217–237, 1986.
- R. E. Reed-Hill. *Trans. of Met. Soc. AIME*, 218:554, 1960.
- C.S. Roberts. *Magnesium and its Alloys*. John Wiley, New York and London, 1960.
- M. Shamsi, M. Sanjari, and A. Zarei Hanzaki. Study of fractional softening of az31 magnesium alloy under multistage hot deformation. *Materials Science and Technology*, 25(8):1039–1045, 2009.
- O. Sitdikov, R. Kaibyshev, and T. Sakai. Dynamic recrystallization based on twinning in coarse-grained mg. *Materials Science Forum*, 419-422:521–526, 2003.

Brian J. Skinner. Earth resources. *Proc. Natl. Acad. Sci*, 76(9):4214–4217, September 1979.

A. Styczynski, Ch. Hartig, J. Bohlen, and D. Letzig. Cold rolling textures in az31 wrought magnesium alloy. *Scripta Materialia*, 50:943–947, 2004.

C. W. Su, L. Lu, and M. O. Lai. Recrystallization and grain growth of deformed magnesium alloy. *Philosophical Magazine*, 88(2):181–200, 2008.

M. Verdier, Y. Brechet, and P. Guyot. Recovery of almg alloys: flow stress and strain-hardening properties. *Acta Materialia*, 47(1):127–134, 1998.

B.C Wonsiewicz and W.A Backofen. Plasticity of magnesium crystals. *Trans. Metall. Soc*, 238:1422–1431, 1967.

Bud Caesar Wonsiewicz. *Plasticity of Magnesium Crystals*. PhD thesis, MIT, 1966.

M. H. Yoo. Slip, twinning, and fracture in hexagonal close-packed metals. *Metal Trans A*, 12A:409–418, 1981.